Automatic surface inspection using wavelet reconstruction

D. M. Tsai and B. Hsiao

Machine Vision Lab.

Department of Industrial Engineering and Management

Yuan-Ze University, Chung-Li, Taiwan, R.O.C.

E-mail: iedmtsai@saturn.yzu.edu.tw

1. INTRODUCTION

Visual inspection makes up an important part of quality control in manufacturing. The manual activity of inspection could be subjective and highly dependent on the experience of human inspectors. In this study, we use machine vision for automatic surface inspection.

In automatic surface inspection, one has to solve the problem of detecting small surface defects which locally break the homogeneity of a texture pattern. Textures are generally classified into two major types, structural and statistical [1]. Structural textures are those that are composed of repetitions of some basic texture primitive, such as directional lines, with a deterministic rule of displacement. This type of texture arises in machined surfaces. Statistical textures cannot be described by primitives and displacement rules. The spatial distribution of gray levels in such textured image is rather stochastic. Sandpaper and leather, for instance, fall in this category.

The inspection task in this paper is classified as qualitative inspection [2] which involves detecting novel but obviously faulty items such as scratches, cracks, stains,

and other ill-defined faults. Many of these unanticipated defects are small in size, and cannot be described by explicit measures, making automatic defect detection difficult.

Most of the defect detection systems are focused on nontextured surfaces such as glass panel [3], sheet steel [4], aluminum strips [5] and web materials [6], using simple thresholding or edge detection techniques. Defects in these images can be easily detected because commonly used measures usually have very distinct values. Automatic visual inspection techniques for textured surfaces generally compute a set of textural features in a sliding window, and search for significant local deviations in the feature values. The most difficult task of this approach is to extract adequate textural features which most completely embody information of the texture in the image. A set of features that is an optimal representation of a specific texture could be completely useless for other texture patterns. There is no straightforward manner to judge the appropriate features to use. Therefore, the selection of an adequate feature set for a new texture in the training process could be very time-consuming and requires the help of human knowledge. Furthermore, textures which are characterized by a vector of multiple features result in high dimensionality. This call for sophisticated classifiers such as Bayes [7], maximum likelihood [8], and neural networks [9] to discriminate texture classes.

A wide spectrum of methods has been proposed to extract textural features either directly from the spatial domain or from the spatial-frequency domain. In the spatial domain, simple textural features are the first-order statistics [10] such as mean, variance, skewness and kurtosis from the gray-level histogram of an image. The more reliable and commonly used features are the second-order statistics derived from spatial gray-level co-occurrence matrices [11]. They have been applied to wood

inspection [12], carpet wear assessment [13] and roughness measurement of machined surfaces [10].

Early work [14] suggested that it may be possible to find better textural features, which are less sensitive to noise and intensity variation, in the spatial-frequency domain. Liu and Jernigan [15] reviewed a set of 28 textural features extracted in the spatial-frequency domain for texture analysis. The reported applications of spatial-frequency methods in texture analysis are mainly limited to texture classification and segmentation [16-18]. These methods generally consider textural feature sets derived from the Fourier domain images and use various classifiers such as distance measures, K-nearest neighbor rules, Bayes probability and neural networks to discriminate textures.

The Fourier transform is a global approach that only characterizes the spatial-frequency distribution, but it does not consider the information in the spatial domain. In the last decade, the multichannel Gabor filters [19-22] are well recognized as a joint spatial/spatial-frequency representation for analyzing textured images with highly specific frequency and orientation characteristics. This technique extracts features by filtering the textured image with a set of Gabor filter banks characterized by the frequency, the orientation of the sinusoid, and the scale of the Gaussian function.

The design of optimal Gabor filters is a very complicated task. Although many methods [23,24] have been developed for the design of filter banks, human intervention is generally required to assist in selecting the appropriate filter parameters for the textures under study. The main problem of Gabor schemes is that if

the center frequency of a selected Gabor filter does not match any of the important harmonics in the textured images, it produces only noisy information and degrades the discrimination performance [25]. Besides, Gabor filtering methods are very computationally expensive since the 2-D convolution must be carried out in a sliding window throughout the entire image.

In the recent past, multiresolution decomposition schemes based on wavelet transforms have received considerable attention as alternatives for the extraction of textural features. The continuous 1-D wavelet transform was initially introduced by Grossmann and Morlet [26]. The 2-D wavelet transform was then defined by Lemarie and Meyer [27]. Its pyramid algorithm implementation was described by Mallat [28]. The multiresolution wavelet representation allows an image to be decomposed into a hierarchy of localized subimages at different spatial frequencies [29]. It divides the 2-D frequency spectrum of an image into a lowpass (smooth) subimage, and a set of highpass (detail) subimages. Compared to the Fourier transform, the wavelet transform is a time-frequency function which describes the information of a signal in various time window and frequency bands. It is particular useful for the analysis of non-stationary or locally irregular signal. Since images in different scales and frequencies have inherently characteristics for the appearance of a texture, the multiresolution, multichannel modeling capability of wavelets is well-suited for texture analysis.

The use of wavelets for texture analysis was pioneered by Mallat [28], who showed that a particular function of the wavelet orthonormal basis is equal to textural primitives with spatial orientation and narrow frequency tuning. Chang and Kuo [30] proposed a tree-structured wavelet transform for texture classification. They used an

energy criterion to select the subimages for further decomposition. A set of textural features is derived from the energy values of dominant channels, and distance measures are then employed to discriminate textures. Pichler *et al.* [25] compared two feature extraction methods based on the pyramid and tree-structured wavelet transforms for texture segmentation. Unser [31] studied texture classification and segmentation problems using wavelet frames. The present analysis methods used an overcomplete wavelet decomposition in which the output of the filter banks is not subsampled. It results in a texture description invariant with respect to translation of the input signal, and improves robustness of texture classification. Laine and Fan [32] used both energy and entropy metrics of each decomposed wavelet packet as textural features. The number of features is numerous. It involves 17 features of a standard wavelets and 341 features of a complete set of wavelet packets. A two-layer neural network uses those features as input for texture classification. Chen and Lee [29] considered the problem of texture segmentation in mammographic images. The image details at different resolutions is first examined using a standard wavelet transform. Contextual information from the wavelet decomposed images is then studied using a nonstationary Gaussian Markov random field. A fuzzy-C-means clustering method is used for segmentation based on the multiresolution and contextual information embedded in the neighborhood of each pixel. Chitre and Dhawan [33] presented an M-band wavelet technique for the classification of natural textures. Compared to the standard 2-band wavelets, M-band wavelets are more suitable for the analysis of high-frequency signals with relatively narrow bandwidth [34]. The M-band wavelet filters are designed using a genetic algorithm. Energy and entropy are computed on each decomposed subband, and the K-nearest neighbor classifier is then used to discriminate textures.

Van de Wouwer *et al*. [35] extended the multiresolution wavelet techniques to color texture classification. Textural features are given by wavelet correlation signatures which contain the energies of each color plane, together with the cross correlation between different color planes. Randen and Husoy [36] reviewed numerous filtering approaches to textural feature extraction. The most major filtering approaches included for comparison are Law mask, ring/wedge filters, eigenfilters, Gabor filter banks, discrete cosine transform, quadrature mirror filters, wavelet transforms, wavelet packets, wavelet frames, etc. The textural features are computed as the local energy of the filter responses. They found no single filtering approach that performs best for all test images. Lambert and Bock [37] proposed a feature extraction approach for texture defect detection. The textural features are derived from the coefficients of wavelet packet decomposition. Feature values are defined by the sum of absolute values of the coefficients in a predetermined neighborhood window with varying sizes in different resolution levels. Neural network and Bayes classifiers are used to evaluate the feature vector. Amet *et al*. [38] presented a defect detection algorithm based on the subband decomposition of images through wavelet filters and extraction of the statistical features from the subband image using co-occurrence matrix techniques. Detection of defects is performed by partitioning the textured image into non-overlapping subwindows and discriminating each subwindow using the Mahalanobis distance measure.

The wavelet transform methods aforementioned for texture analysis are generally based on the extraction of textural features in different scales and subbands. An important problem in wavelet texture analysis is that the number of features tends to become huge. This calls for sophisticated classifiers working in high dimensional feature spaces. In addition, most techniques proposed for segmenting textured images

involve the use of a neighborhood window with predetermined size to exploit local characteristics. Different textures may need different window sizes, and the repetitive computation in a sliding window throughout the entire image tends to slow the detection efficiency.

In this paper, we propose a multiresolution approach based on an image restoration technique using the analysis and synthesis wavelet transforms for inspecting surface defects in both structural and statistical textures. The proposed method does not rely on textural features to detect local anomalies. It alleviates all limitations of feature extraction schemes aforementioned.

The multiresolution wavelet technique transforms images into a representation in which both spatial and frequency information present. It is ideally suited for describing local changes in a homogeneous textured image. For one level of standard wavelet decomposition, we obtain one smooth subimage and three detail subimages which contain fine structures with horizontal, vertical and diagonal orientations. By properly selecting the smooth subimage or the combination of detail subimages in different resolution levels for backward wavelet transform, the reconstructed image will remove regular, repetitive texture patterns and enhance only local anomalies. A simple thresholding can then be used to discriminate between defective regions and homogeneous regions in the reconstructed image. This converts the difficult defect detection problem in complicated textured images into a simple thresholding problem in nontextured images.

This paper is organized as follows: Section 2 first reviews the 1-D wavelet transform, and then introduces the 2-D inverse wavelet transform for image

restoration. Image-restoration strategies based on the selection of the smooth subimage or the detail subimages with specific directional structures for statistical and structural textures are discussed. Orthogonal and biorthogonal basis functions used for wavelet filtering are also addressed in this section. Section 3 presents the experimental results on a variety of structural and statistical textures including machined surfaces, natural wood, textile fabrics, sandpaper and leather. Effects of different wavelet bases, number of multiresolution levels, subimage restoration strategies, and changes in image rotation are evaluated thoroughly in this section. This paper is concluded in Section 4.

2. WAVELET ANALYSIS FOR DEFECT DETECTION

2.1 Review of 1-D wavelet transforms

We start with the brief review of 1-D wavelet transform. The wavelet transform is defined as a decomposition of a signal $f(t)$ with a family of real orthonormal bases $\psi_{j,k}(t)$ generated from a kernel function $\psi(t)$ by dilations and translations [39,40].

$$\psi_{j,k}(t) = 2^{-j/2}\psi(2^{-j}t - k)$$

where j and k are integers. The mother wavelet $\psi(t)$ has to satisfy

$$\int \psi(t)dt = 0$$

Since $\psi_{j,k}(t)$ forms an orthonormal set, the wavelet coefficients of the signal $f(t)$ can be calculated by the inner product

$$a_{j,k} = \langle f(t), \psi_{j,k}(t) \rangle = \int f(t) \cdot \psi_{j,k}(t)dt$$

For the wavelet expansion, signal $f(t)$ can be reconstructed via

$$f(t) = \langle a_{j,k}, \psi_{j,k}(t) \rangle = \sum_{j,k} a_{j,k} \cdot \psi_{j,k}(t)$$

The multiresolution formulation needs two closely related basic functions. In addition to the mother wavelet $\psi(t)$, we will need another basic function, called the scaling function $\phi(t)$. $\phi(t)$ can be expressed in terms of a weighted sum of shifted $\phi(2t)$ as [41] :

$$\phi(t) = \sqrt{2} \sum_n l(n) \cdot \phi(2t - n) \qquad (1)$$

where $l(n)'s$ are the scaling (lowpass) coefficients, and the $\sqrt{2}$ maintains the norm of the scaling function with the scale of two. The scaling coefficients $l(n)$ must satisfy

$$\sum_n l(n) = \sqrt{2}$$

and

$$\sum_n l(n) \cdot l(n - 2k) = \begin{cases} 1 & if \ k = 0 \\ 0 & otherwise \end{cases}$$

The dilation equation above (eq.(1)) is fundamental to the theory of scaling functions. The mother wavelet $\psi(t)$ is related to the scaling function via

$$\psi(t) = \sqrt{2} \sum_n h(n)\phi(2t - n) \qquad (2)$$

where $h(n)'s$ are the wavelet (highpass) coefficients. They are required by orthogonality to be related to the scaling coefficients by

$$h(n) = (-1)^n l(1 - n)$$

The mother wavelet $\psi(t)$ is good at representing the detail and high-frequency parts of a signal. The scaling function $\phi(t)$ is good at representing the smooth and low-frequency parts of the signal.

In most practical applications, one never explicitly calculates the scaling function

9

$\phi(t)$ and wavelet $\psi(t)$, but performs the transform using the scaling coefficients $l(n)$ and the wavelet coefficients $h(n)$. In forward wavelet analysis, a J-level discrete decomposition can be written as

$$f(t) = \sum_n c_{0,n} \phi(t-n)$$

$$= \sum_k c_{J,k} \phi_{J,k}(t) + \sum_{j=1}^{J} \sum_k d_{j,k} \psi_{j,k}(t) \qquad (3)$$

where coefficients $c_{0,n}$ are given, and coefficients $c_{j,k}$ and $d_{j,k}$ at resolution j are related to the coefficients $c_{j-1,k}$ at level $j-1$ by the following recursive equations [40] :

$$c_{j,k} = \sum_n c_{j-1,k} l(n-2k) \qquad (4a)$$

and

$$d_{j,k} = \sum_n c_{j-1,k} h(n-2k) \qquad (4b)$$

for $j = 1,2,...,J$.

In the expansion above (eq. (3)), the first summation gives a function that is a low resolution or coarse approximation of $f(t)$, Which represents the smooth part of $f(t)$. For each increasing level j in the second summation, a higher or fine resolution function is added, which represents the detail part of $f(t)$. Eqs. 4(a) and 4(b) show that the scaling and wavelet coefficients at different levels of scale can be obtained by convolving the expansion coefficients at scale $j-1$ by the time-reversed recursion coefficients $l(-n)$ and $h(-n)$, then down-sampling (taking every other term) to give the expansion coefficients at the next level of j.

In backward wavelet synthesis, a reconstruction of the original fine scale coefficients of the signal can be made from a combination of the scaling coefficients

and wavelet coefficients at a coarse resolution. Because all of these functions are orthonormal, we have

$$c_{j,k} = \sum_n c_{j+1,n} l(k - 2n) + \sum_n d_{j+1,n} h(k - 2n) \tag{5}$$

The synthesis operation of eq.(5) is equivalent to up-sampling the coefficients $c_{j+1,n}$ and $d_{j+1,n}$ (inserting a zero between each of the original terms) in the coarser level j+1, and then convolving with $l(n)$ and $h(n)$, individually, to obtain the scaling coefficients in the finer level j. The synthesis process can be recursively continued to the original level. The analysis and synthesis procedures lead to the pyramid-structured wavelet decomposition [28].

2.2 2-D wavelet reconstruction

The 1-D multiresolution wavelet decomposition can be easily extended to two dimensions by introducing separable 2-D scaling and wavelet functions as the tensor products of their one-dimensional complements. Hence, we obtain

$$\phi_{LL}(x, y) = \phi(x) \cdot \phi(y)$$

$$\psi_{LH}(x, y) = \phi(x) \cdot \psi(y)$$

$$\psi_{HL}(x, y) = \psi(x) \cdot \phi(y)$$

$$\psi_{HH}(x, y) = \psi(x) \cdot \psi(y)$$

The 2-D wavelet analysis operation consists of filtering and down-sampling horizontally using 1-D lowpass filter L (with impulse responses $l(i)$) and highpass filter H (with impulse responses $h(j)$) to each row in the image $f(x, y)$, and

produces the coefficient matrices $f_L(x, y)$ and $f_H(x, y)$. Vertically filtering and down-sampling follows, using the lowpass and highpass filters L and H to each column in $f_L(x, y)$ and $f_H(x, y)$, and produces 4 subimages $f_{LL}(x, y)$, $f_{LH}(x, y)$, $f_{HL}(x, y)$ and $f_{HH}(x, y)$ for one level of decomposition. $f_{LL}(x, y)$ is a smooth subimage, which represents the coarse approximation of the image. $f_{LH}(x, y)$, $f_{HL}(x, y)$ and $f_{HH}(x, y)$ are detail subimages, which represent the horizontal, vertical and diagonal directions of the image. Figure 1 depicts 1 stage in a multiresolution pyramid decomposition of an image. Figure 2 shows the decomposition result of 2 multiresolution levels, where $f^{(i)}(x, y)$ represents the decomposed subimage at resolution level i. The detailed 2-D pyramid decomposition algorithm, with periodic boundary conditions applied, can be expressed as follows :

Let $M \times N =$ the original image size of $f(x, y)$

$l(i) =$ the analysis lowpass coefficients of a specific wavelet basis, $i = 0,1,2,\ldots,N_l$ - 1, where N_l is the support length of the filter L.

$h(j) =$ the analysis highpass coefficients of a specific wavelet basis, $j = 0,1,2,\ldots,N_h - 1$, where N_h is the support length of the filter H.

Then,

$$f_L(x, y) = \frac{1}{N_l} \sum_{i=0}^{N_l-1} l(i) \cdot f((2x+i) \bmod M, y)$$

$$f_H(x, y) = \frac{1}{N_h} \sum_{j=0}^{N_h-1} h(j) \cdot f((2x+j) \bmod M, y)$$

for $x = 0,1,2,\ldots,\dfrac{M}{2} - 1$ and $y = 0,1,2,\ldots,N - 1$.

$$f_{LL}(x, y) = \frac{1}{N_l} \sum_{i=0}^{N_l-1} l(i) \cdot f_L(x, (2y+i) \bmod N) \tag{6a}$$

$$f_{LH}(x,y) = \frac{1}{N_h} \sum_{j=0}^{N_h-1} h(j) \cdot f_L(x,(2y+j) \bmod N) \tag{6b}$$

$$f_{HL}(x,y) = \frac{1}{N_l} \sum_{i=0}^{N_l-1} l(i) \cdot f_H(x,(2y+i) \bmod N) \tag{6c}$$

$$f_{HH}(x,y) = \frac{1}{N_h} \sum_{j=0}^{N_h-1} h(j) \cdot f_H(x,(2y+j) \bmod N) \tag{6d}$$

for $x = 0,1,2,\ldots,\dfrac{M}{2}-1$ and $y = 0,1,2,\ldots,\dfrac{N}{2}-1$.

The 2-D pyramid algorithm can iterate on the smooth subimage $f_{LL}(x,y)$ to obtain four coefficient matrices in the next decomposition level.

The inverse 2-D wavelet transform can be implemented using a backward 2-D pyramid algorithm. The 2-D wavelet synthesis operation consists of up-sampling and filtering vertically using 1-D synthesis lowpass filter $\tilde{L}$ (with impulse responses $\tilde{l}(i)$) and highpass filter $\tilde{H}$ (with impulse responses $\tilde{h}(j)$) to each column in the subimage. The results are added. Horizontal up-sampling and filtering then follows, using the lowpass and highpass filters $\tilde{L}$ and $\tilde{H}$, to each row of the reversed image. Figure 3 shows 1 stage in a wavelet reconstruction. In this study, we do not want to completely restore the textured image under inspection with 100% accuracy. Rather, we would like to eliminate all regular, repetitive textures in the reconstructed image by selecting proper smooth or detail subimages for wavelet synthesis. Therefore, the reconstructed subimages are not added in the intermediate synthesis levels. The summation operation of the selective reconstructed-subimages is only performed at the original level (level 0).

The detailed 2-D wavelet synthesis procedure for each of the four decomposed subimages $f_{LL}(x, y)$, $f_{LH}(x, y)$, $f_{HL}(x, y)$ and $f_{HH}(x, y)$ is individually described as follows :

Let $R \times C =$ the size of a subimage to restore

$\tilde{l}(i) =$ the synthesis lowpass coefficients of a specific wavelet basis,

$i = 0,1,2,\ldots,N_{\tilde{l}}$, where $N_{\tilde{l}}$ is the support length of the filter $\tilde{L}$.

$\tilde{h}(j) =$ the synthesis highpass coefficients of a specific wavelet basis,

$j = 0,1,2,\ldots,N_{\tilde{h}}$, where $N_{\tilde{h}}$ is the support length of the filter $\tilde{H}$.

1. The synthesis of the smooth subimage $f_{LL}(x, y)$

Upsample $f_{LL}(x, y)$ by a factor of 2 along the y-axis and filter with lowpass filter $\tilde{L}$:

Let $f_{S_y}(x, 2y) = f_{LL}(x, y)$ and $f_{S_y}(x, 2y + 1) = 0$,

for $x = 0,1,2,\ldots,R - 1$ and $y = 0,1,2,\ldots,C - 1$.

$$f_{S_y}^{-1}(x, y) = \frac{1}{N_{\tilde{l}}} \sum_{i=0}^{N_{\tilde{l}}-1} \tilde{l}(i) \cdot f_{S_y}(x, (y + i) \bmod 2C)$$

Upsample $f_{S_y}^{-1}$ by a factor of 2 along the x-axis and filter with lowpass filter

$\tilde{L}$:

Let $f_{S_x}^{-1}(2x, y) = f_{S_y}^{-1}(x, y)$ and $f_{S_x}^{-1}(2x + 1, y) = 0$

for $x = 0,1,2,\ldots,R - 1$ and $y = 0,1,2,\ldots,2C - 1$.

$$f_S(x, y) = \frac{1}{N_{\tilde{l}}} \sum_{i=0}^{N_{\tilde{l}}-1} \tilde{l}(i) \cdot f_{S_x}^{-1}((x+i) \bmod 2R, y) \tag{7a}$$

2. The synthesis of the horizontal detail subimage $f_{LH}(x, y)$

Upsample $f_{LH}(x, y)$ along the y-axis and filter with highpass filter $\tilde{H}$:

Let $f_{h_y}(x, 2y) = f_{LH}(x, y)$ and $f_{h_y}(x, 2y+1) = 0$,

for $x = 0, 1, 2, \ldots, R\text{-}1$ and $y = 0, 1, 2, \ldots, C\text{-}1$.

$$f_{h_y}^{-1}(x, y) = \frac{1}{N_{\tilde{h}}} \sum_{j=0}^{N_{\tilde{h}}-1} \tilde{h}(j) f_{h_y}(x, (y+j) \bmod 2C)$$

Upsample $f_{h_y}^{-1}$ along the x-axis and filter with lowpass filter $\tilde{L}$:

Let $f_{h_x}^{-1}(2x, y) = f_{h_y}^{-1}(x, y)$ and $f_{h_x}^{-1}(2x+1, y) = 0$,

for $x = 0, 1, 2, \ldots, R\text{-}1$ and $y = 0, 1, 2, \ldots, 2C\text{-}1$.

$$f_h(x, y) = \frac{1}{N_{\tilde{l}}} \sum_{i=0}^{N_{\tilde{l}}-1} \tilde{l}(i) f_{h_x}^{-1}((x+i) \bmod 2R, y) \tag{7b}$$

The vertical and diagonal detail subimages $f_{HL}(x, y)$ and $f_{HH}(x, y)$ can be reconstructed in a similar way as $f_{LH}(x, y)$ with corresponding filtering operations ($\tilde{L}$ in column first, and then $\tilde{H}$ in row for $f_{HL}(x, y)$; $\tilde{H}$ in both column and row for $f_{HH}(x, y)$) to obtain the restored images $f_v(x, y)$ and $f_d(x, y)$, respectively.

2.3 Selection of wavelet bases and subimages for reconstruction

In this study, we evaluate both orthogonal and biorthogonal bases used to design the analysis filters L and H and synthesis filters $\tilde{L}$ and $\tilde{H}$. A central reason to use a particular basis function is to match the characteristics of the underlying texture.

An orthogonal basis function must satisfy [40] :

$$\int \phi_{J,k}(t) \cdot \phi_{J,k'}(t)dt = \delta_{kk'} \tag{8a}$$

$$\int \psi_{j,k}(t) \cdot \phi_{J,k'}(t)dt = 0 \tag{8b}$$

$$\int \psi_{j,k}(t) \cdot \psi_{j',k'}(t)dt = \delta_{jj'} \cdot \delta_{kk'} \tag{8c}$$

where
$$\delta_{ij} = \begin{cases} 1 & if \ i = j \\ 0 & otherwise \end{cases}$$

Biorthogonal wavelets were first introduced by Cohen *et al*. [42]. In this construction, orthonormal wavelets are generalized by using two sets of functions $\phi_{j,k}$, $\psi_{j,k}$ and their dual $\tilde{\phi}_{j,k}$, $\tilde{\psi}_{j,k}$. Biorthogonal wavelets are not orthogonal and do not satisfy the orthogonality relationship in eqs. 8(a)-8(c). However, they do satisfy the following biorthogonal relationships :

$$\int \phi_{J,k}(t) \cdot \tilde{\phi}_{J,k'}(t)dt = \delta_{kk'} \tag{9a}$$

$$\int \psi_{j,k}(t) \cdot \tilde{\phi}_{J,k'}(t)dt = 0 \tag{9b}$$

$$\int \psi_{j,k}(t) \cdot \tilde{\psi}_{j',k'}(t)dt = \delta_{jj'} \cdot \delta_{kk'} \tag{9c}$$

Symmetric wavelets and scaling functions are made possible in the framework of biorthogonal bases, and they do not introduce phase shifts in the coefficients. The coefficients of the synthesis filters $\tilde{L}$ and $\tilde{H}$ are derived from the dual wavelet functions :

$$\tilde{l}(n) = \frac{1}{\sqrt{2}} \int \tilde{\phi}(t) \cdot \tilde{\phi}(2t - n)dt$$

$$\tilde{h}(n) = \frac{1}{\sqrt{2}} \int \tilde{\psi}(t) \cdot \tilde{\phi}(2t - n)dt$$

The analogue to $h(n) = (-1)^n l(1-n)$ is

$$h(n) = (-1)^n \tilde{l}(1-n) \tag{10a}$$

$$\tilde{h}(n) = (-1)^n l(1-n) \tag{10b}$$

For the orthogonal wavelets, the synthesis filters $\tilde{L}$ and $\tilde{H}$ are the same as the analysis ones L and H.

There are no simple rules for selecting a wavelet to use for a specific analysis. Evaluation of all wavelet basis functions is beyond the limit of the experiments. However, we study a few popular orthogonal wavelets including :

1. Haar [43] : the only symmetric exact reconstruction filter with the shortest support length of 2.

2. Daublets [44] : the first type of continuous orthogonal wavelets with compact support. Two Daublets families D4 and D12 are considered, where the number represents the length of support. Daublets are asymmetric bases.

3. Symmlets [44] : the Symmlets wavelets are constructed to be as nearly symmetric as possible. Two Symmlets families S8 and S20 are considered, where the number also represents the support length.

For biorthogonal wavelets, we consider two families of B-spline polynomial functions [42] : BS2.2 and BS3.9, where the first number indicates the degree of the polynomial for the wavelets, and the second number indicates the support length of the dual wavelet. The coefficient values [40,45] of the analysis filters L and H and the synthesis filters $\tilde{L}$ and $\tilde{H}$ for the seven wavelet bases aforementioned are listed in the appendix.

Three important factors for wavelet selection are the smoothness, the spatial

localization and the frequency localization. In general, the wavelets with wider support are smoother and have better frequency localization, but are spatially less localized. In terms of computational complexity, the wavelet support should be short. However, it cannot be too short to prevent noise and block effect in the restored image.

The wavelet synthesis procedure described in section 2.2 can be recursively applied to any subimage from its coarsest level to the finest level. Denote $W^{-1}(f^{(i)})$ by the iteration of inverse wavelet transformation of a subimage f from multiresolution level i to level 0. In this study, defects in both structural and statistical textures are investigated. In general, structural textures are anisotropic and statistical textures are isotropic. We propose two synthesis strategies to enhance the defects in the restored image. The first synthesis strategy is to reconstruct only the smooth subimage $f_{LL}^{(J)}$ at a proper resolution level J. Since a statistical texture is isotropic, reconstructing a smooth subimage at its coarser resolution will remove (or blur) all regular, repetitive texture patterns (lowpass signals), and reserve only the local anomalies (highpass signals) in the restored image.

The second synthesis strategy is to reconstruct some selective detail subimages. A decomposition in octave bands yields three detail subimages with horizontal, vertical and diagonal directions. Since a structural texture may present high directionality, reconstructing the detail subimages with direction emphasis different from that of the regular texture will remove all repetitive, directional patterns in the original image, and preserve only local anomalies in the restored image. For instance, given a machined surface with vertical feed marks in the image, reconstructing only horizontal detail subimages $f_{LH}^{(i)}$ and diagonal detail subimages $f_{HH}^{(i)}$ at resolution levels $1, 2, ..., J$, i.e.,

$$\sum_{i=1}^{J}\left[W^{-1}(f_{LH}^{(i)}) + W^{-1}(f_{HH}^{(i)})\right],$$

will remove all vertical feed marks in the restored image. The repetitive, directional pattern will result in an approximately uniform gray level, whereas the local anomalies will yield distinct gray levels in the restored image.

In this paper, we are considering a supervised surface inspection problem. Supervised systems are common in machine vision and are appropriate for controlled circumstances in manufacturing. The number of multiresolution levels and the decomposed subimages used for image reconstruction are predetermined from a texture model. The impact of wavelet bases, number of multiresolution levels and subimage synthesis strategies on detection results are empirically evaluated in the following section.

3. EXPERIMENTAL RESULT

In this section, we present the experimental results on a variety of structural and statistical textures found in industry to evaluate the performance of the proposed defect detection method. All experiments are implemented on a personal computer. The images are 256×256 pixels wide with 8-bit gray levels.

In the proposed method, there are three main factors that may affect the inspection results : 1) selection of wavelet bases, 2) selection of the number of multiresolution levels, and 3) selection of decomposed subimages for reconstruction. Besides these, the effect of changes in image rotation is also evaluated in this section.

3.1 Selection of wavelet bases

In this experiment, we evaluate five orthogonal wavelet bases including Haar, Daublets D4 and D12, Symmlets S8 and S20, and two B-spline biorthogonal wavelet bases BS2.2 and BS3.9. Figure 4(a) shows a structural texture with repetitive vertical line pattern and an irregular "Z" defect. Figures 4(b)-4(h) display the restoring results from wavelet bases Haar, D4, D12, S8, S20, BS2.2 and BS3.9, respectively, based on the selective horizontal detail subimages $f_{LH}^{(i)}$ and diagonal detail subimages $f_{HH}^{(i)}$ in three multiresolution levels, i.e.,

$$\hat{f}(x, y) = \sum_{i=1}^{3} \left[W^{-1}(f_{LH}^{(i)}) + W^{-1}(f_{HH}^{(i)}) \right]$$

The image $\hat{f}(x, y)$ restored from horizontal and diagonal detail subimages remove all vertical lines in the original image and preserve only the edges of the defect "Z". The defect in the restored image can be efficiently separated from the background using a simple binary thresholding technique such as the one proposed by Otsu [46]. The binary thresholding results of Figures 4(b)-4(h) are demonstrated in Figures 5(a)-5(g), respectively.

Figure 6(a) shows a structural texture of wood with repetitive, horizontal stripes. Figures 6(b)-6(h) display the restoring results from the seven wavelet bases based on the selective vertical and diagonal detail subimages $f_{HL}^{(i)}$ and $f_{HH}^{(i)}$ in three multiresolution levels, i.e.,

$$\hat{f}(x, y) = \sum_{i=1}^{3} \left[W^{-1}(f_{HL}^{(i)}) + W^{-1}(f_{HH}^{(i)}) \right]$$

The binary thresholding results of Figures 6(b)-6(h) are presented in Figures 7(a)-7(g).

Figure 8(a) shows a statistical texture of sandpaper with a scratched "A". Figure 9(a) shows one additional statistical texture of sandpaper with a wear defect. The restoring results of Figure 8(a) and Figure 9(a) from the seven wavelet bases are, respectively, displayed in Figures 8(b)-8(h) and Figures 9(b)-9(h). Both statistical textures use the smooth subimage at resolution level 3 for reconstruction, i.e.,

$$\hat{f}(x, y) = W^{-1}(f_{LL}^{(3)})$$

The binary thresholding results of Figures 8(b)-8(h) and Figures 9(b)-9(h) are presented in Figures 10(a)-10(g) and Figures 11(a)-11(g), respectively.

It can be seen from Figure 4 through Figure 11 that the choice of wavelet bases has only small effects on the detection results for structural textures, and all wavelet bases can enhance the defects in the restored images. However, orthogonal wavelets generally outperform biorthogonal wavelets since biorthogonal wavelets lack of orthogonality properties. The B-spline biorthogonal wavelets used in statistical textures cannot sufficiently capture all defect pixels (Figures 10(f) and 10(g)), or they generate noisy effect (Figure 11(f) and 11(g)). For a given orthogonal wavelet function, the basis with longer support may not generate better detection result (such as D12 *vs.* D4 or S20 *vs.* S8). The longer supports may oversmooth the local anomalies, and are less computationally efficient, compared to the shorter supports. The Haar wavelet has a very compact support of 2. It works well for structural textures with high directionality (restoring detail subimages), but performs poorly for statistical textures (restoring the smooth subimage) due to the block effect as shown in Figures 8(b) and 9(b). Based on the consideration of both detection effectiveness and computational efficiency, orthogonal wavelet bases with compact support length such

as D4 and S8 are the best choice for the application of defect detection in textured surfaces.

3.2 Selection of multiresolution levels

One of the most important aspects of texture is scale. The fine and coarse resolution components capture the fine and coarse scale features in the image. Decomposition of a textured image in its proper resolution will effectively highlight the local anomalies in the homogeneous surface.

The two sandpaper textures shown in Figures 8(a) and 9(a) are used to evaluate the impact of varying number of multiresolution levels on the reconstruction result. Figures 12(b)-12(f) and Figures 13(b)-13(f) present the restoration results from resolution levels 2, 3, 4, 5 and 6 for Figures 12(a) and 13(a), respectively. All these images are soly reconstructed from the smooth subimage, i.e., $W^{-1}(f_{LL}^{(J)})$, with the wavelet basis S8. Both Figures 12 and 13 reveal that too small the number of multiresolution levels (such as $J = 2$) cannot sufficiently separate defects from the repetitive texture pattern. However, too large the number of multiresolution levels (such as $J \geq 5$) yields the fusion effect of the anomalies, any may result in false detection. The number of multiresolution levels between 3 and 4 is most appropriate to enhance defects in the restored image. Experiments on a variety of textures images have cinfirmed that 3 multiresolution levels are generally sufficient for defect detection applications.

3.3 Selection of decomposed subimages for reconstruction

For each textured image, we can select either the smooth subimage or some specific detail subimages for reconstruction. All images in this experiment are reconstructed with wavelet basis S8 in 3 multiresolution levels. Figures 14(a) and 15(a) show two vertical-line textures, one containing a line defect, and the other containing blob defects. The restoration results from the smooth subimage, i.e., $W^{-1}(f_{LL}^{(3)})$, for figures 14(a) and 15(a) are presented in Figures 14(b) and 15(b), respectively. The restoration results from the direct sum of horizontal and diagonal detail subimages, i.e.,

$$\sum_{i=1}^{3}\left[W^{-1}(f_{LH}^{(i)}) + W^{-1}(f_{HH}^{(i)})\right]$$

for Figures 14(a) and 15(a) are presented in Figures 14(d) and 15(d). For structural textures with high directionality, the restoration results as shown in Figures 14 an 15 reveal that the selective detail subimages can effectively remove all repetitive line patterns, and enhance the edges of defects in the restored image. However, residuals of repetitive lines remain in the restored image if the smooth subimage is selected for reconstruction. Therefore, reconstructing selective detail subimages is preferred for enhancing defects in structural textures with high directionality.

Figures 16(a) and 17(a) show two statistical textures of sandpaper. Restoration results from the smooth subimage, i.e., $W^{-1}(f_{LL}^{(3)})$, are presented in Figures 16(b) and 17(b), respectively. Restoration results from the direct sum of all three detail subimages, i.e.,

$$\sum_{i=1}^{3}\left[W^{-1}(f_{LH}^{(i)}) + W^{-1}(f_{HL}^{(i)}) + W^{-1}(f_{HH}^{(i)})\right]$$

are displayed in Figures 16(d) and 17(d). For statistical textures with isotropic patterns, it can be seen from Figures 16 and 17 that reconstructing detail subimages cannot enhance the defects in the restored images, and no defects are detected in the corresponding binary images (Figures 16(e) and 17(e)). Reconstructing the smooth subimages can effectively enhance the defect regions in the restored image, and it well separates defects from the background in the corresponding binary images (Figures 16(c) and 17(c)). Therefore, reconstructing the smooth subimage is preferred for enhancing defects in statistical textures.

3.4 The effect of changes in image rotation

In this study, textured image can be reconstructed from either the smooth subimage or the selective detail subimages. Since a smooth subimage is a coarse approximation of the original fine image, varying rotational angle of the test image will not affect the restoration result. However, the three detail subimages represent the directional information of a texture in horizontal, vertical and diagonal directions. Given a set of predetermined detail subimages, the restoration result is sensitive to the change in image rotation.

All images used in this experiment are reconstructed with wavelet basis S8 in 3 multiresolution levels. Figure 18 show a statistical texture of sandpaper in three different orientations. Figures 19(a)-19(f) present the restoration results from the smooth subimages, i.e., $W^{-1}(f_{LL}^{(3)})$, and the corresponding binary results. It can be seen from Figure 19 that the restoration based on the smooth subimage is rotation-invariant. All defects are reliably detected, regardless of the image orientation. Figure 20 shows a line-structured texture in three different orientations. Given that

only horizontal and diagonal detail subimages are used for reconstruction, i.e.,

$$\sum_{i=1}^{3}\left[W^{-1}(f_{LH}^{(i)})+W^{-1}(f_{HH}^{(i)})\right],$$

the corresponding restoration results of Figures 20(a)-20(c) are demonstrated in Figures 21(a)-21(c), respectively. Since the vertical detail subimages are not included in the reconstruction, all vertical lines in Figure 20(a) are completely removed in the restored image as shown in Figure 21(a). However, the repetitive line patterns in Figures 20(b) and 20(c) are not in vertical direction. The reconstruction procedure using detail subimages f_{LH} and f_{HH} preserve the repetitive lines, along with the defects in the restored images as seen in Figures 21(b) and 21(c). Therefore, the reconstruction of highly structural textures from selective detail subimages are sensitive to image rotation.

Bases on the experimental results discussed above, we can conclude that in the application of wavelet transforms for defect detection in textured images :

1) orthogonal wavelet bases with compact support length such as D4 or S8 are preferred in order to avoid leakage of subtle anomalies and have fast computation (but it cannot be too short to ensure sufficient smoothness).

2) the number of multiresolution levels between 3 and 4 is generally sufficient to remove regular, repetitive textures and enhance defects in the restored image.

3) reconstruct only the smooth subimage for statistical textures, and restore the detail subimages which have different directional emphasis with respect to that of the repetitive pattern for structural textures with explicit directionality. Note that

smooth-subimage reconstruction is rotation-invariant. Detail-subimage reconstruction is rotation-dependent and, therefore, the orientation of a structural texture must be known *a priori* or predetermined.

In order to demonstrate the effectiveness of the proposed wavelet reconstruction scheme with the suggested selections above for defect detection, a few more textures found in industry are also examined. All subsequent test samples are reconstructed with wavelet basis S8 in three multiresolution levels.

Figure 22(a) shows a milled surface in vertical lay direction. The reconstruction result shown in Figure 22(b) is obtained from the horizontal and diagonal detail subimages, i.e.,

$$\sum_{i=1}^{3}\left[W^{-1}(f_{LH}^{(i)})+W^{-1}(f_{HH}^{(i)})\right]$$

Note that the subtle scratch is reliably separated in the binary image as shown in Figure 22(c). Figure 23(a) shows a natural wood image. The reconstruction result shown in Figure 23(b) is based on the vertical and diagonal detail subimages, i.e.,

$$\sum_{i=1}^{3}\left[W^{-1}(f_{HL}^{(i)})+W^{-1}(f_{HH}^{(i)})\right]$$

The line pattern in wood is less regular than that in the machined surface. However, the defect in wood is also reliably separated in the binary image as shown in Figure 23(c).

Figures 24(a) and 24(b) present two textile fabrics. The reconstruction results shown in Figures 24(c) and 24(d) are obtained from the smooth-subimages, i.e., $W^{-1}(f_{LL}^{(3)})$ for both fabrics. Since the textile fabrics do not explicitly show clear lines

on the surfaces, the smooth subimages instead of the detail subimages are used for reconstruction. The stain and shedding defects in the fabrics are well separated in the binary images as shown in Figures 24(e) and 24(f). Figure 25(a) shows a leather image. The restored image shown in Figure 25(b) is obtained from the smooth subimage, i.e., $W^{-1}(f_{LL}^{(3)})$, and the defect is well captured in the binary image as shown in Figure 25(c).

4. CONCLUSIONS

In this paper we have considered the problem of detecting local defects embedded in a homogeneous texture. Since local defects exhibit no distinct textural properties, this task is clearly different from segmentation by texture. Classical texture segmentation techniques need to extract a set of textural features for each image pixel defined in a neighborhood window and use high-dimensional classifiers to discriminate between pixels in the textured image. The proposed method does not rely on local textural features in a pixel-by-pixel basis. It is based on an image restoration scheme using the multiresolution wavelet transforms, and results in considerable computational savings. With proper selection of a smooth subimage or detail subimages in different multiresolution levels for image reconstruction, the global repetitive texture pattern can be effectively removed and local anomalies can be enhanced in the restored image. A simple binary thresholding is therefore used to separate the defective regions from the homogeneous regions in the restored image.

The effectiveness of the proposed wavelet reconstruction scheme is determined by the wavelet bases, the number of multiresolution levels and the decomposed subimages used for reconstruction. The experimental results have revealed that

orthogonal wavelet bases are more appropriate than biorthogonal bases for the application of defect detection in textured surfaces. Orthogonal wavelet bases that are sufficiently compact are preferred to capture local deviations in homogeneous textured surfaces. Too large the number of multiresolution levels causes the fusion effect of defects in the restored image, whereas too small the number of multiresolution levels cannot completely separate defective regions from the homogeneous regions. The number of multiresolution levels between 3 and 4 is generally well-suited for most textures to capture local anomalies in the restored image. For statistical textures, only the smooth subimage, which represents the coarse approximation of the original image, needs to be included in the reconstruction to enhance the defects in the restored image. The reconstruction from a smooth subimage is rotation-invariant and, therefore, the test image can be presented in arbitrary directions. For structural textures with high directionality, the selective detail subimages, which have different direction emphasis from the original repetitive pattern, are included in the reconstruction to remove all repetitive textures. The reconstruction from selective detail subimages is rotation-dependent and, therefore, the direction of the test image must be fixed or predetermined.

Since the proposed method is a supervised one, the number of multiresolution levels and the decomposed subimages used for reconstruction must be manually predetermined for each texture class. The task of automatic selection of the number of multiresolution levels and the decomposed subimages for the best enhancement of defects and removals of repetitive texture patterns based on the gray-level variance in the restored image and the energy in each decomposed subimage is currently under investigation.

REFERENCE

1. A. Pikaz and A. Averbuch, An efficient topological characterization of gray-levels textures using a multiresolution representation, Graphical Models and Image Processing 59 (1997) 1-17.

2. T. S. Newan and A. K. Jain, A survey of automated visual inspection, Computer Vision and Image Understanding 61(1995) 231-262.

3. J. Wilder, Finding and evaluating defects in glass, in Machine Vision for Inspection and Measurement (Ed. H. Freeman), Academic Press, New York (1989) 237-255.

4. J. Olsson and S. Gruber, Web process inspection using neural classification of scattering light. Proceedings of the IEEE International Conference on Industrial Electronics, Control, Instrumentation and Automation (IECON'92), San Diego (1992) 1443-1448.

5. C. Fernandez, C. Platero, P. Campoy and R. Aracil, Vision system for on-line surface inspection in aluminum casting process, Proceedings of the IEEE International Conference on Industrial Electronics, Control, Instrumentation and Automation (IECON'93), Maui, HA (1993) 1854-1859.

6. D. Brzakovic and N. Vujovic, Designing defect classification system: a case study, Pattern Recognition 29 (1996) 1401-1419.

7. R. C. Gonzalez and R. E. Woods, Digital Image Processing, Addison-Wesley, Reading, Mass. (1992).

8. F. S. Cohen, Maximum likelihood unsupervised textured image segmentation, GVGIP : Graphical Models and Image Processing 54 (1992) 239-251.

9. M. M. Van Hulle and T. Tollenaere, A modular artificial neural network for texture processing, Neural Networks 6 (1993) 7-32.

10. K. V. Ramana and B. Ramamoorthy, Statistical methods to compare the texture features of machined surfaces, Pattern Recognition 29 (1996) 1447-1459.

11. R. M. Haralick, K. Shanmugam and I. Dinstein, Texture features for image classification, IEEE Trans. System, Man Cybernet. 3 (1973) 610-621.

12. R. W. Conners, C. W. McMillin, K. Lin and R. E. Vasquez-Espinosa, Identifying and locating surface detects in wood, IEEE Trans. Pattern Anal. Mach. Intell. PAMI-5 (1983) 573-583.

13. L. H. Siew and R. M. Hogdson, Texture measures for carpet wear assessment, IEEE Trans. Pattern Anal. Mach. Intell. 10 (1988) 92-105.

14. H. Wechsler, Texture analysis: a survey, Signal Processing 2 (1980) 271-282.

15. S. -S. Liu and M. E. Jernigan, Texture analysis and discrimination in additive noise, Computer Vision, Graphics, Image Process. 49 (1990) 52-67.

16. M. F. Augusteijn and L. E. Clemens, A performance evaluation of texture measures for image classification and segmentation using cascade-correlation architecture, IEEE International Conference on Neural Networks and IEEE World Congress on Computational Intelligence 7 (1994) 4300-4305.

17. R. Azencott, J. -P. Wang and L. Younes, Texture classification using windowed Fourier filters, IEEE Trans. Pattern Anal. Mach. Intell. 19 (1997) 148-153.

18. H. Arof and F. Deravi, Circular neighborhood and 1-D DFT features for texture classification and segmentation, IIE Proceedings-Vision, Image and Signal Processing 145 (1998) 167-172.

19. M. Porat and Y. Y. Zeevi, The generalized Gabor scheme of image representation in biological and machine vision, IEEE Trans. Pattern Anal. Mach. Intell. 10 (1988) 452-468.

20. A. Teuner, O. Pichler and B. J. Hosticka, Unsupervised texture segmentation of images using tuned matched Gabor filters, IEEE Trans. Image Processing 4 (1995) 863-870.

21. P. P. Raghu and B. Yegnanarayana, Segmentation of Gabor-filtered textures using deterministic relaxation, IEEE Trans. Image Processing 5 (1996) 1625-1636.

22. T. J. Randen and J. H. Husoy, Filtering for texture classification : a comparative study, IEEE Trans. Pattern Anal. Mach. Intell. 21 (1999) 291-310.

23. D. Dunn and W.E. Higgins, Optimal Gabor filters for texture segmentation, IEEE Trans. Image Processing 4 (1995) 947-964.

24. T. P. Weldon, W. E. Higgins and D. F. Dunn, Efficient Gabor filter design for texture segmentation, Pattern Recognition 29 (1996) 2005-2015.

25. O. Pichler, A. Teuner and B. J. Hosticka, A comparison of texture feature extraction using adaptive Gabor filtering, pyramidal and tree structured wavelet transforms, Pattern Recognition 29 (1996) 733-742.

26. A. Grossmann and J. Morlet, Decomposition of Hardy functions into square integrable wavelets of constant shape, SIAM J. Math. 15 (1984) 723-736.

27. P. G. Lemarie and Y. Meyer, Ondelettes et bases Hilbertiennes, Revista Matematica Ibero Americana 2 (1986) 1-18.

28. S. G. Mallat, A theory for multiresolution signal decomposition: the wavelet representation, IEEE Trans. Pattern Anal. Mach. Intell. 11 (1989) 674-693.

29. C. H. Chen and G. G. Lee, On digital mammogram segmentation and microcalcification detection using multiresolution wavelet analysis, Graphical Models and Image Processing 59 (1997) 349-364.

30. T. Chen and C.-C. J. Kuo, Texture analysis and classification with tree-structured wavelet transform, IEEE Trans. Image Processing 2 (1993) 429-441.

31. M. Unser, Texture classification and segmentation using wavelet frames, IEEE Trans. Image Processing 4 (1995) 1549-1560.

32. A. Laine and J. Fan, Texture classification by wavelet packet signatures, IEEE Trans. Pattern Anal. Mach. Intell. 15 (1993) 1186-1191.

33. Y. Chitre and A. P. Dhawan, M-band wavelet discrimination of natural textures, Pattern Recognition 32 (1999) 773-789.

34. P. Steffen, P. N. Heller, R. A. Gopinath, C. S. Burrus, Theory of regular M-band wavelets bases, IEEE Trans. Signal Processing 41 (1993) 3497-3510.

35. G.Van de Wouwer, P. Scheunders, S. Livens and D. Van Dyck, Wavelet correlation signatures for color texture characterization, Pattern Recognition 32 (1999) 433-451.

36. T. Randen and J. H. Husoy, Filtering for texture classification: a comparative study, IEEE Trans. Pattern Anal. Mach. Intell. 21 (1999) 291-310.

37. G. Lambert and F. Bock, Wavelet methods for texture defect detection, IEEE International Conference on Image Processing V.3 (1997) 201-204.

38. A. L. Amet, A. Ertuzun and A. Ercil, Texture defect detection using subband domain co-occurrence matrices, Image Analysis and Interpretation 1 (1998) 205-210.

39. M. Antonini, M. Barlaud, P. Mathieu and I. Daubechies, Image coding using wavelet transform, IEEE Trans. Image Processing 1 (1992) 205-220.

40. C. S. Burrus, R. A. Gopinath and H. Guo, Introduction to Wavelets and Wavelet Transforms: A Primer, Prentice-Hall, Upper Saddle River, NJ, 1998.

41. I. Daubechies, Orthonormal bases of compactly supported Wavelets, Comm. Pure and Applied. Math. 41 (1998) 909-996.

42. A. Cohen, I. Daubechies and J. Feauveau, Bi-orthogonal bases of compactly supported wavelets, Comm. Pure and Applied Math. 45 (1992) 485-560.

43. A. Haar, Zur theorie der orthogonalen Funktionensysteme, Mathematische Annalen 69 (1910) 331-371.

44. I. Daubechies, Ten Lectures on Wavelets, SIAM, philadelphia, PA, 1992.

45. A. Bruce and H.-Y. Gao, Applied Wavelet Analysis with S-PLUS, Springer, New York, NY, 1996.

46. N. Otsu, A threshold selection method for gray-level histograms, IEEE Trans. Systems, Man, Cybernet. 9 (1979) 62-66.
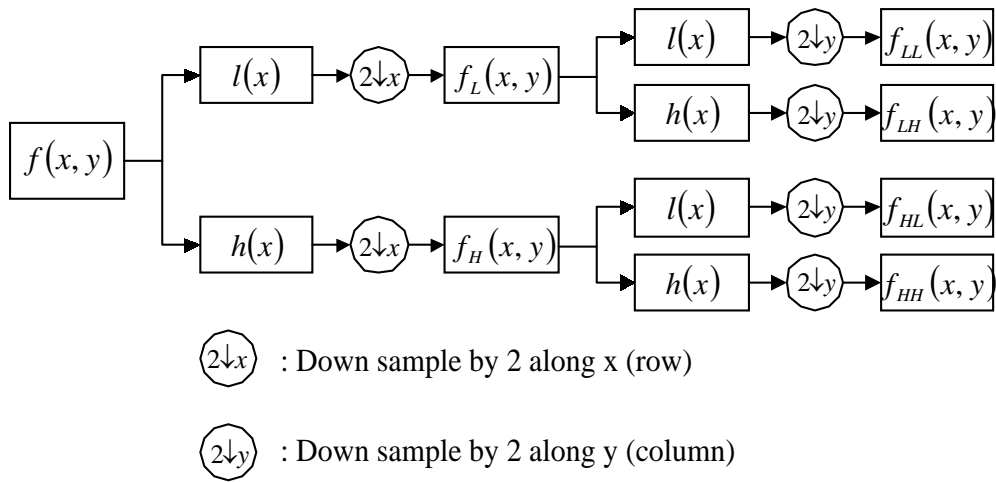
Figure 1. One stage in a multiresolution image decomposition (forward wavelet analysis).

Figure 2. A representation of 2-level image decomposition.
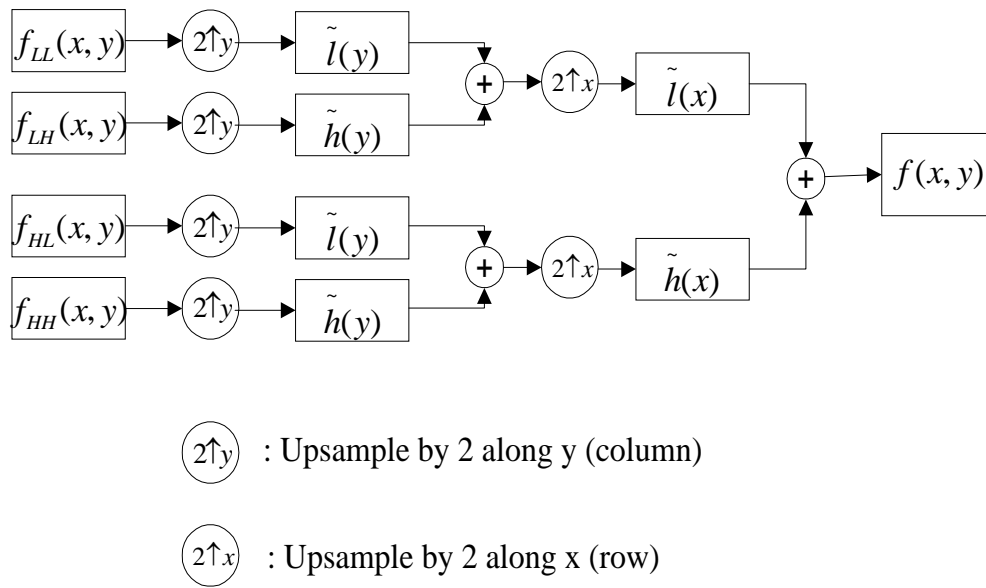
Figure 3.   One stage in a multiresolution image reconstruction (backward wavelet synthesis).

(a) Original image

(b) Haar

(c) D4

(d) D12

(e) S8

(f) S20

(g) BS2.2

(h) BS3.9
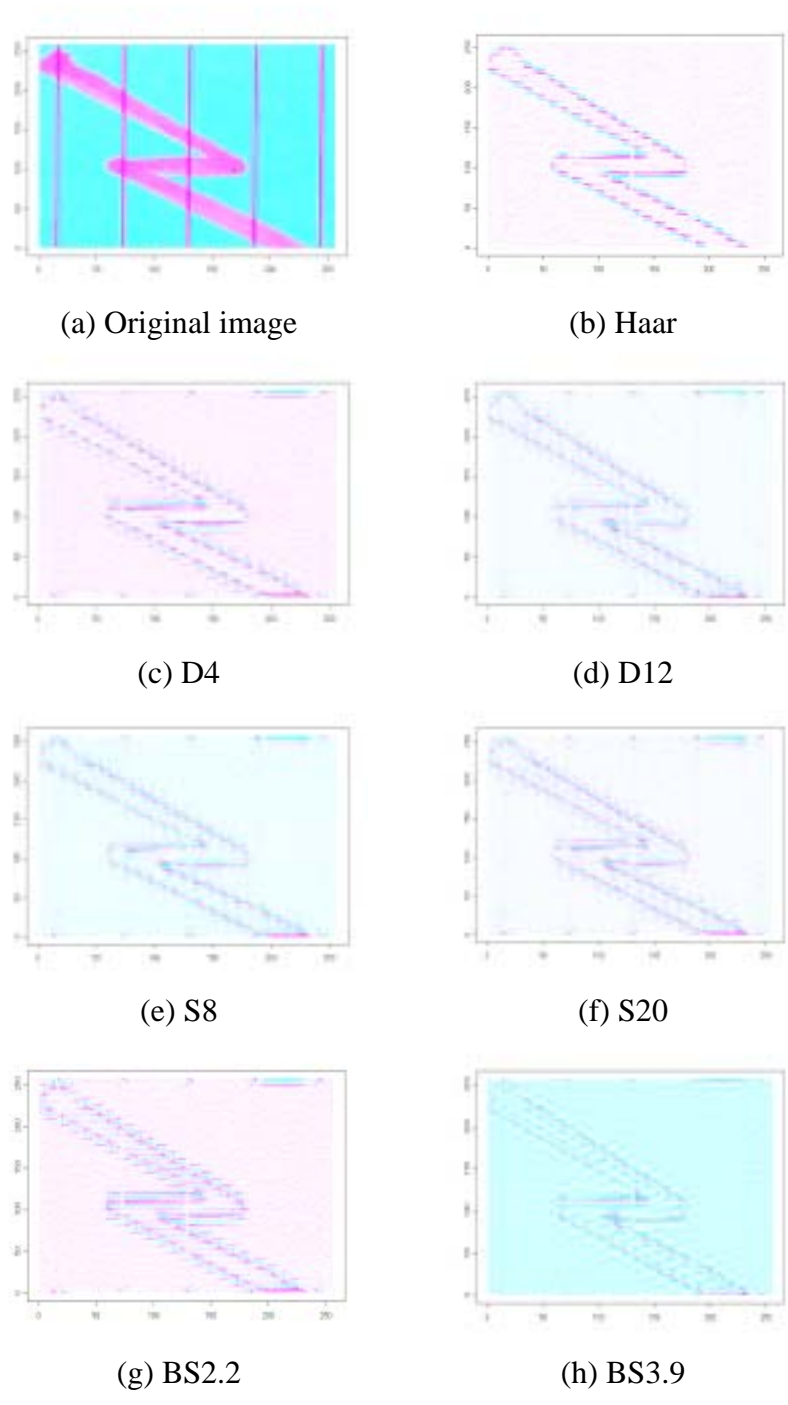
Figure 4.   The effect of various wavelet bases on image reconstruction for a line-texture : (a) the original textured image ; (b) – (h) reconstruction results from wavelet bases Haar, D4, D12, S8, S20, BS2.2 and BS3.9, respectively. (These images are reconstructed from the horizontal and diagonal detail subimages in three multiresolution levels.)

(a) Haar

(b) D4

(c) D12

(d) S8
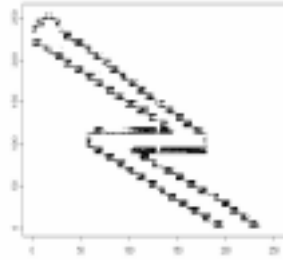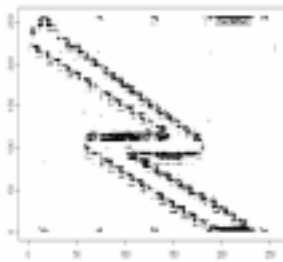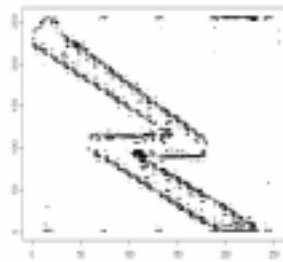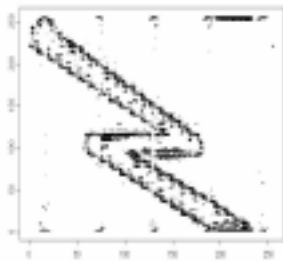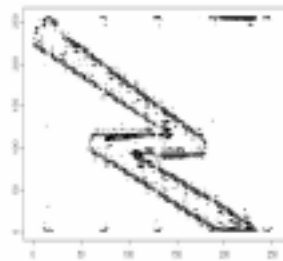
(e) S20
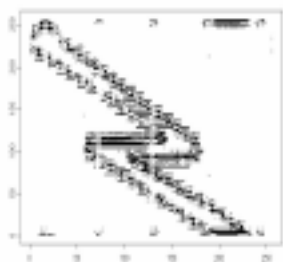
(f) BS2.2
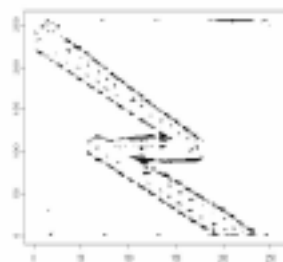
(g) BS3.9

Figure 5. (a) – (g) Binary thresholding results of the reconstructed images shown in Figures 4(b) – 4(h), respectively.

(a) Original image

(b) Haar

(c) D4

(d) D12

(e) S8

(f) S20

(g) BS2.2

(h) BS3.9
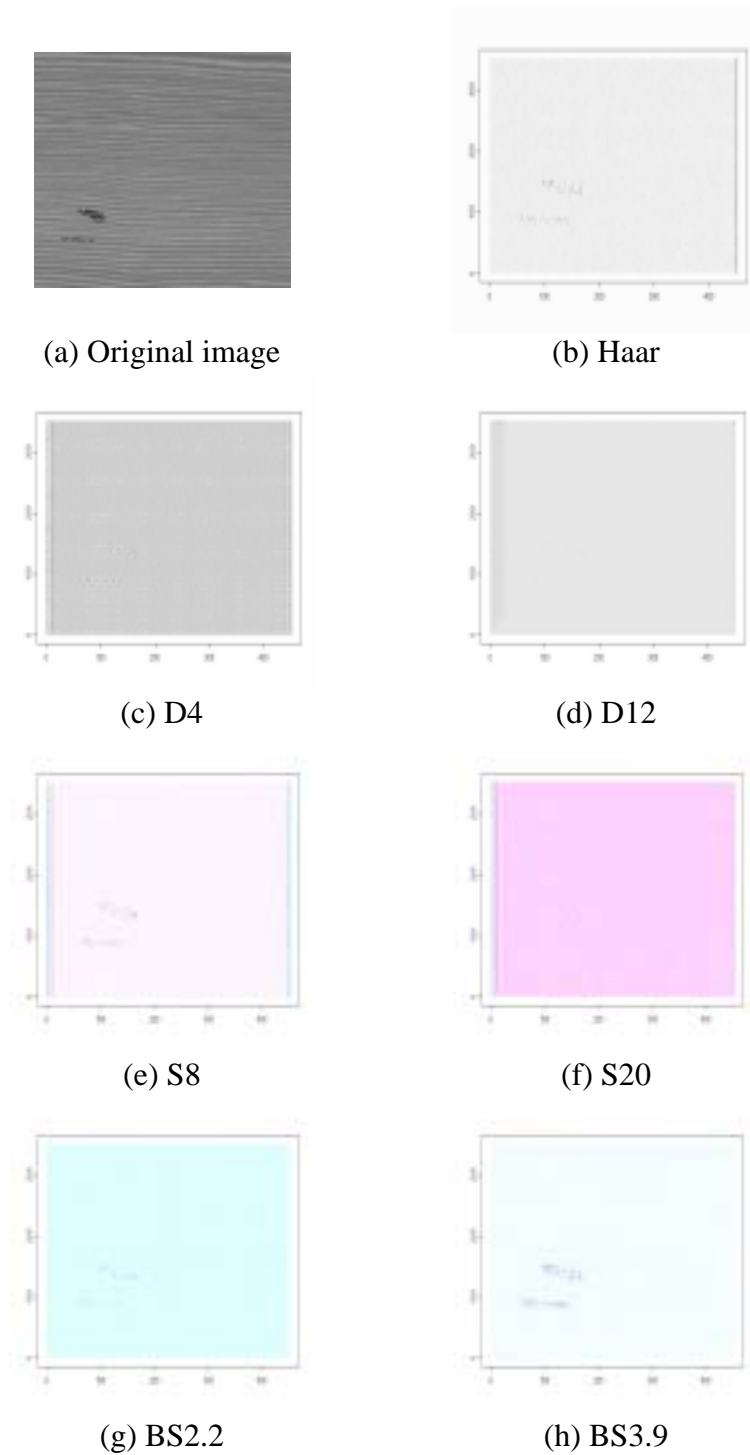
Figure 6. The effect of various wavelet bases on image reconstruction for a wood-texture : (a) the original textured image ; (b) – (h) reconstruction results from wavelet bases Haar, D4, D12, S8, S20, BS2.2 and BS3.9, respectively. (These images are reconstructed from the vertical and diagonal detail subimages in three multiresolution levels.)

(a) Haar

(b) D4

(c) D12

(d) S8

(e) S20

(f) BS2.2

(g) BS3.9
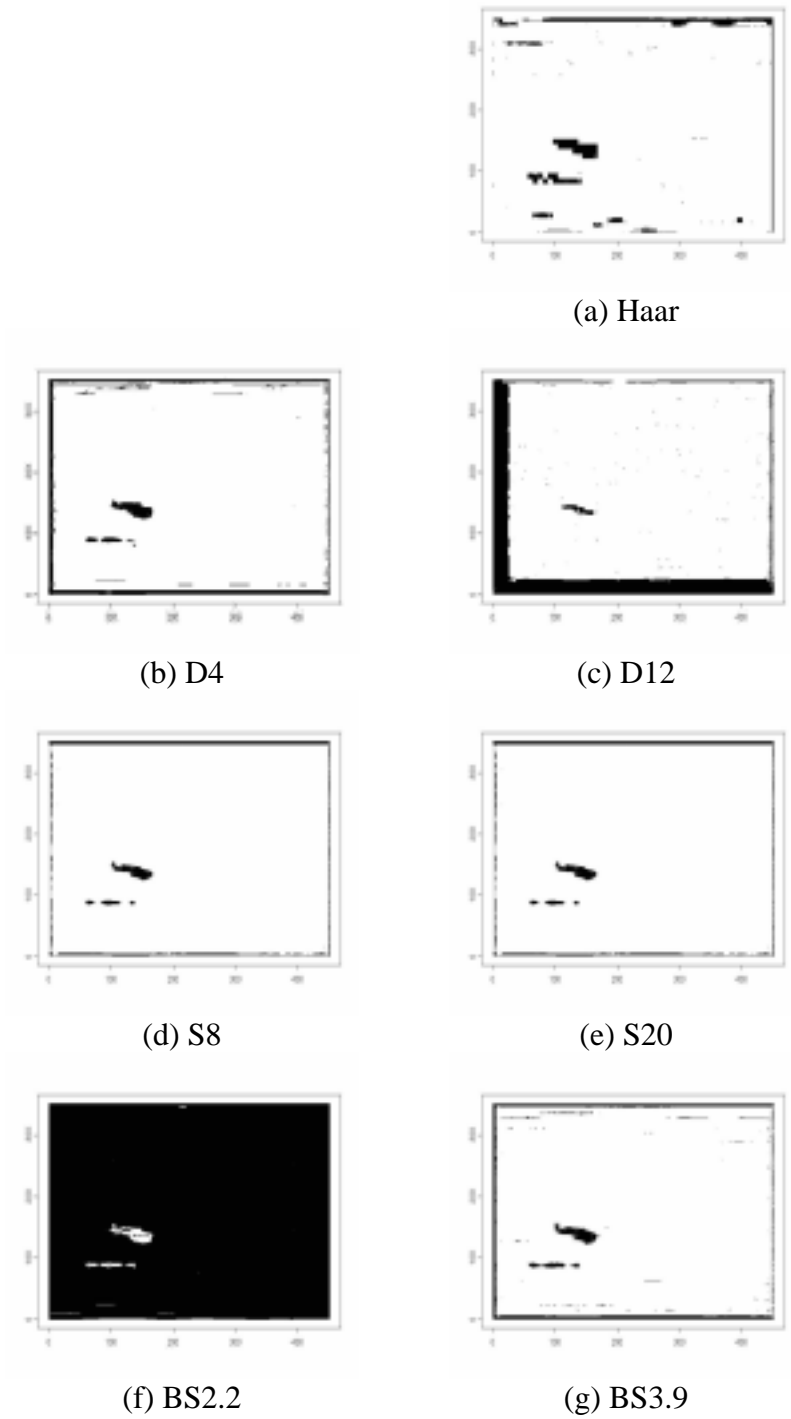
Figure 7. (a) – (g) Binary thresholding results of the reconstructed images shown in Figures 6(b) – 6(h), respectively.

(a) Original image

(b) Haar

(c) D4

(d) D12

(e) S8

(f) S20

(g) BS2.2

(h) BS3.9
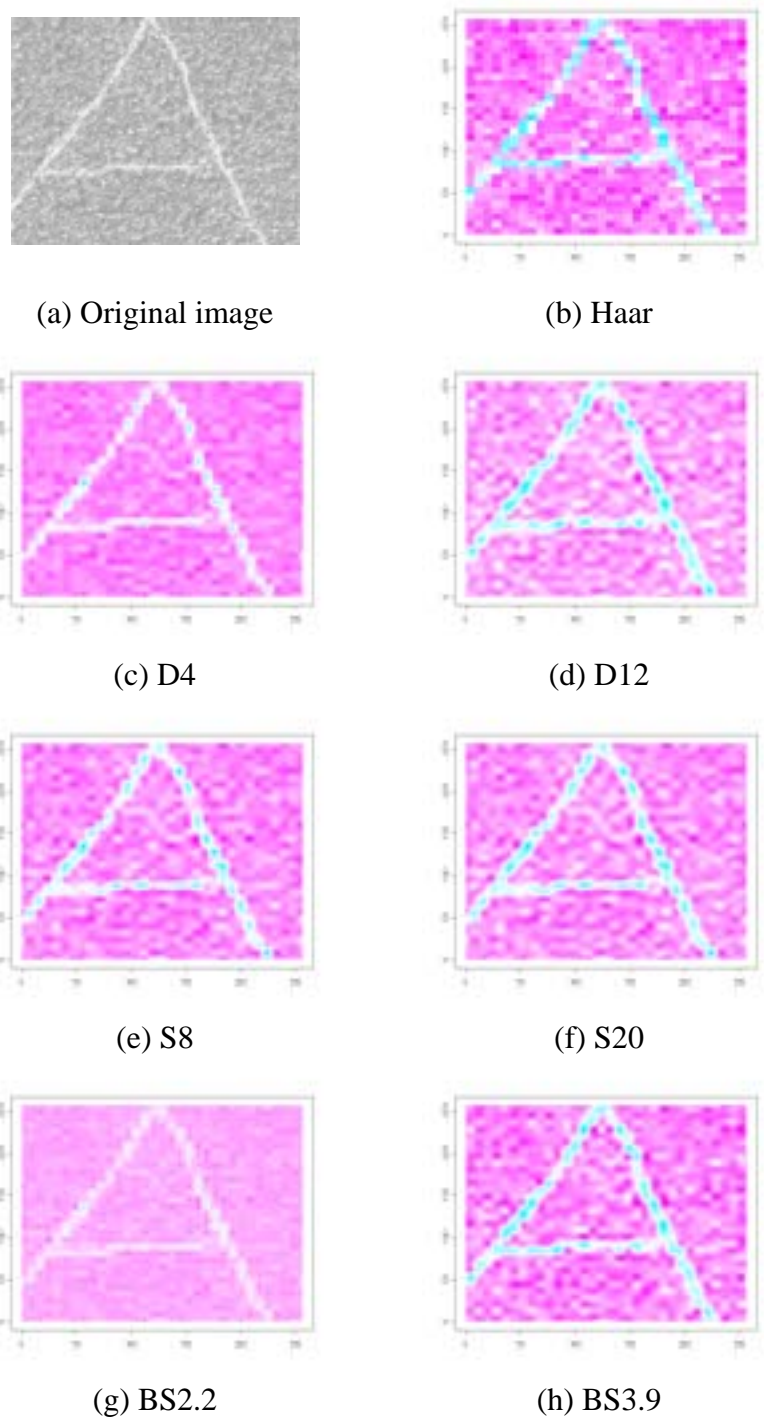
Figure 8. The effect of various wavelet bases on image reconstruction for a sandpaper surface with scratch defects : (a)the original image; (b)–(h) reconstruction results from wavelet bases Haar, D4, D12, S8, S20, BS2.2 and BS3.9, respectively. (These images are reconstructed from the smooth subimages at the third resolution level.)

(a) Original image

(b) Haar

(c) D4

(d) D12

(e) S8

(f) S20

(g) BS2.2

(h) BS3.9
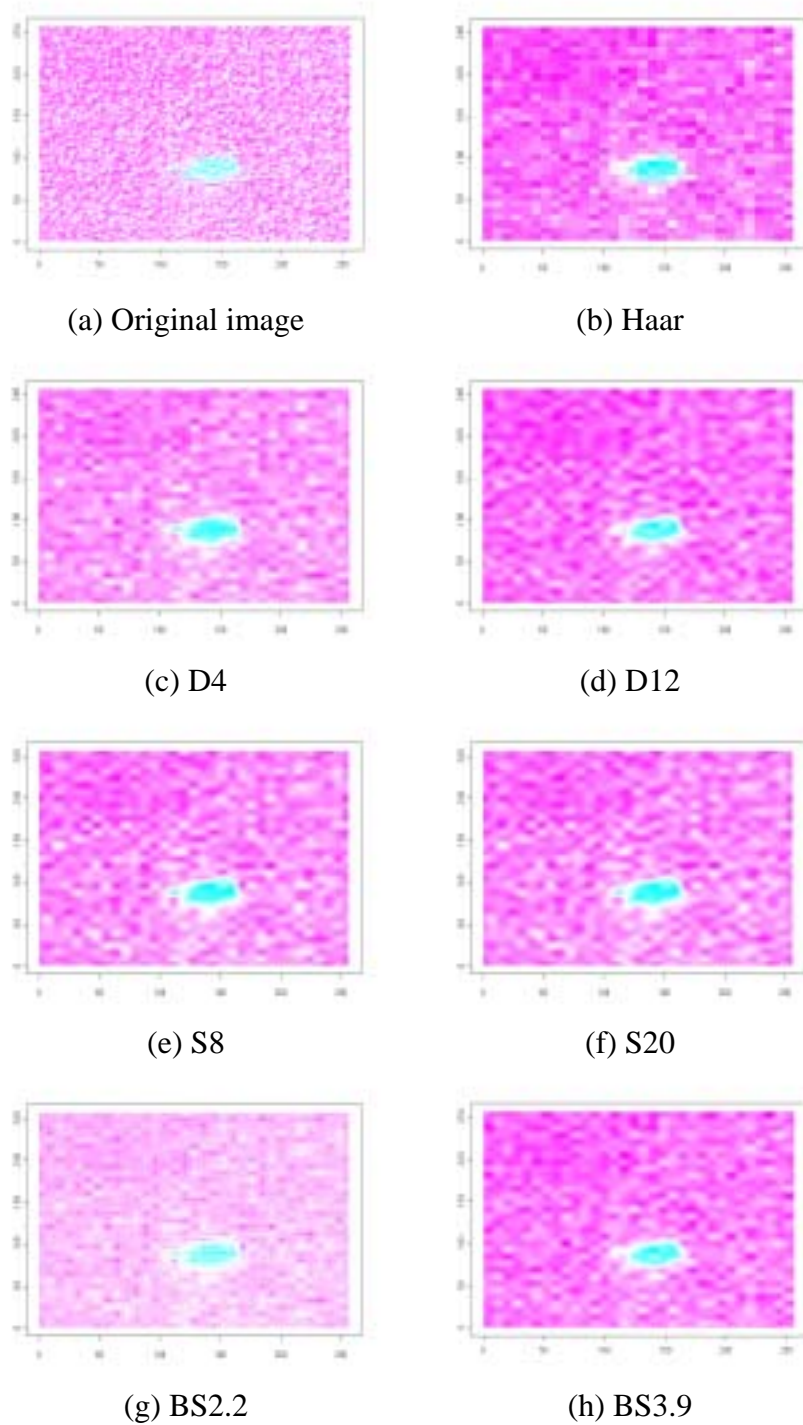
Figure 9. The effect of various wavelet bases on image reconstruction for a sandpaper surface with the wear defect : (a)the original image; (b)–(h) reconstruction results from wavelet bases Haar, D4, D12, S8, S20, BS2.2 and BS3.9, respectively. (These images are reconstructed from the smooth subimages at the third resolution level.)

(a) Haar

(b) D4

(c) D12

(d) S8
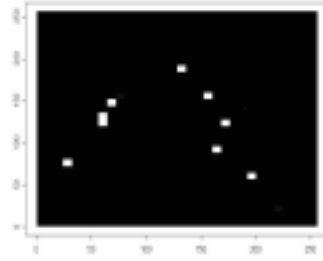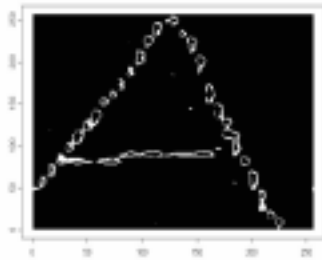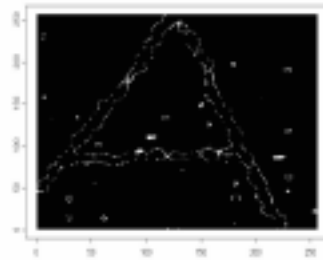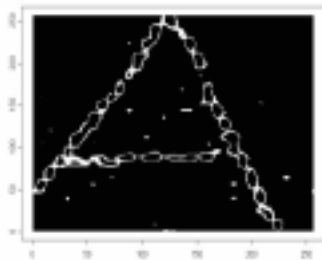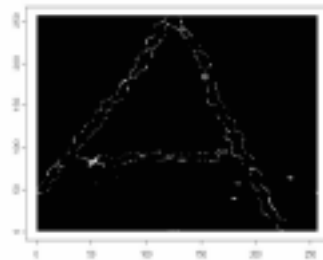
(e) S20
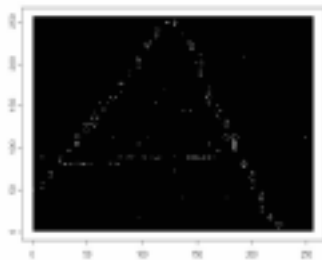
(f) BS2.2
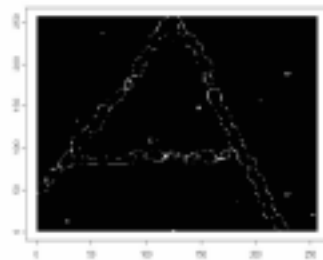
(g) BS3.9

Figure 10.   (a) – (g) Binary thresholding results of the reconstructed images shown

in Figures 8(b) – 8(h), respectively.

(a) Haar

(b) D4

(c) D12

(d) S8

(e) S20

(f) BS2.2

(g) BS3.9
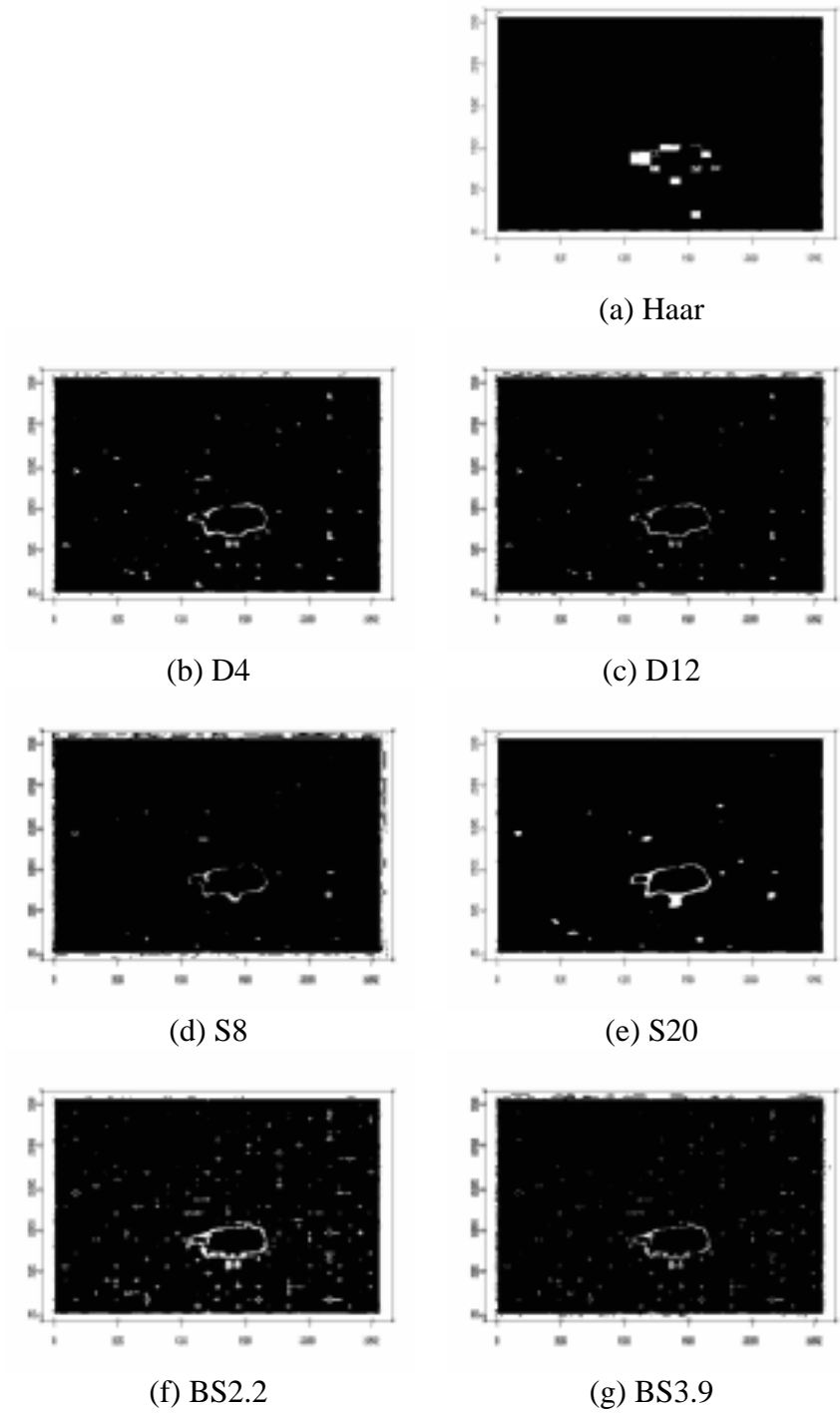
Figure 11.   (a) – (g) Binary thresholding results of the reconstructed images shown in

Figures 9(b) – 9(h), respectively.

(a) Original image

(b) J=2

(c) J=3
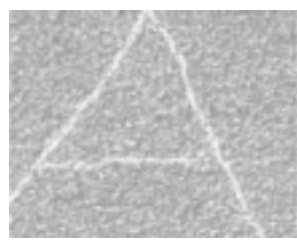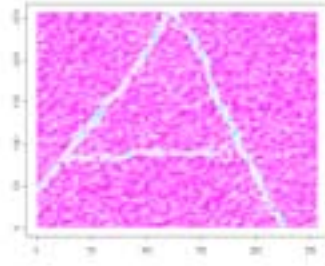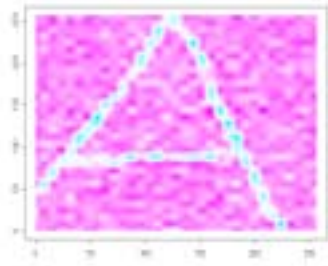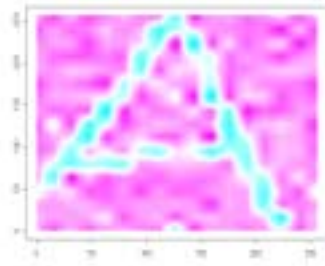
(d) J=4
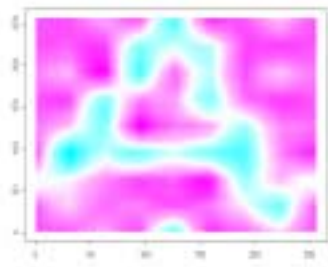
(e) J=5
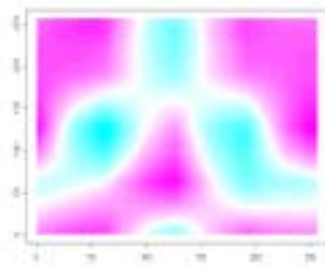
(f) J=6

Figure 12. The effect of various number of multiresolution levels on image reconstruction : (a) the original sandpaper image with scratch defects ; (b) – (f) reconstruction results from multiresolution levels J = 2, 3, 4, 5 and 6, respectively. (The reconstruction is based on the smooth subimage with wavelet basis S8.)

(a) Original image

(b) J=2

(c) J=3

(d) J=4

(e) J=5

(f) J=6
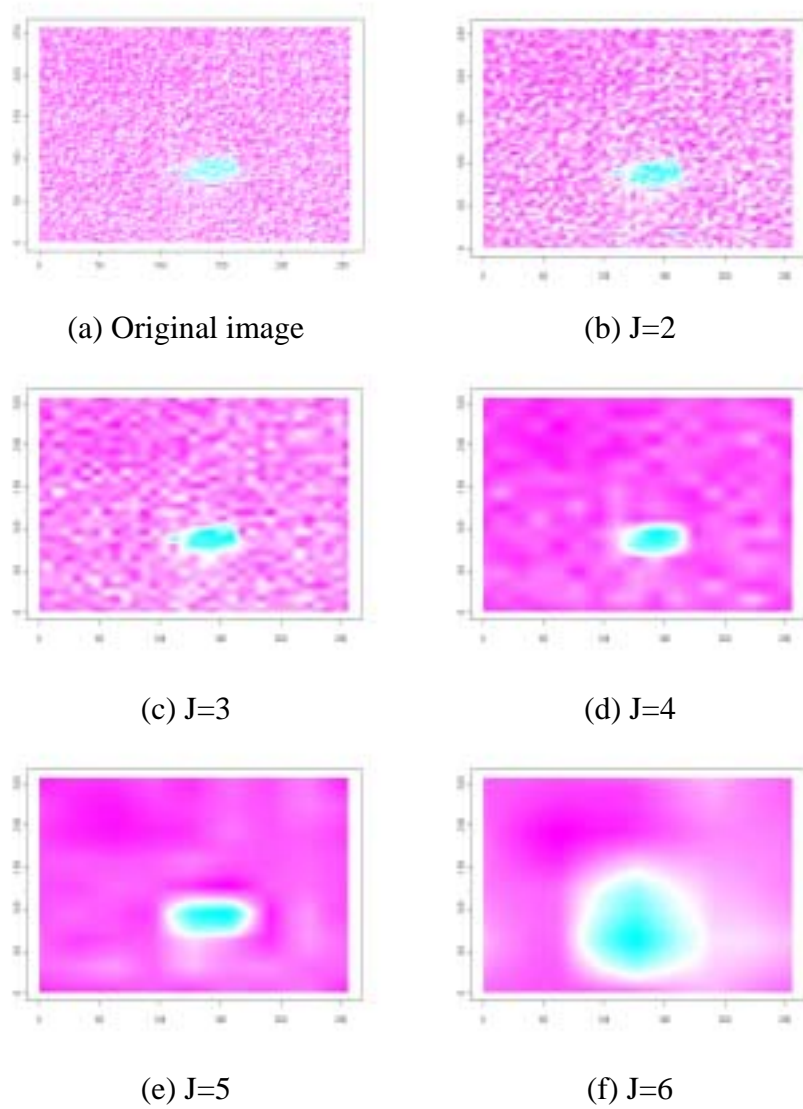
Figure 13. The effect of various number of multiresolution levels on image reconstruction : (a) the original sandpaper image with a wear defect ; (b) – (f) reconstruction results from multiresolution levels J = 2, 3, 4, 5 and 6, respectively. (These images are reconstructed from the smooth subimages with wavelet basis S8.)
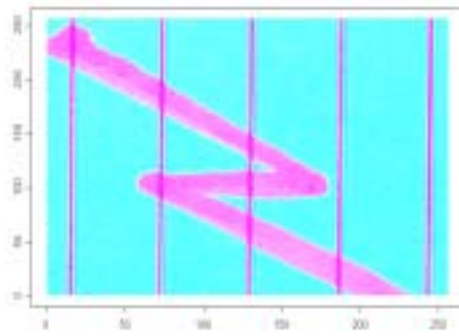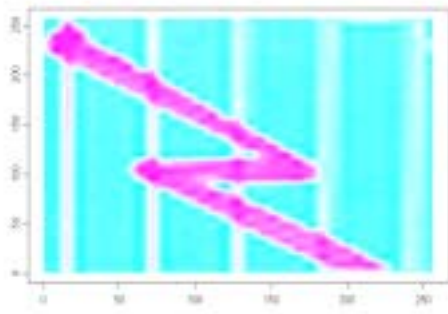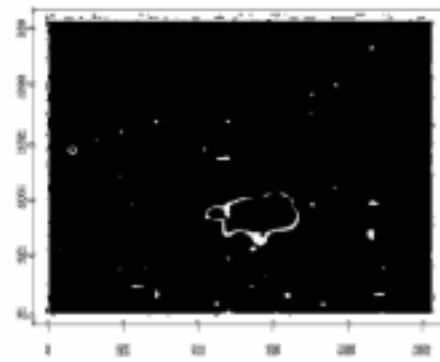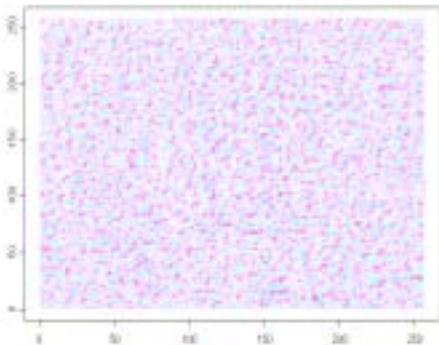
(a) Original image

(b)
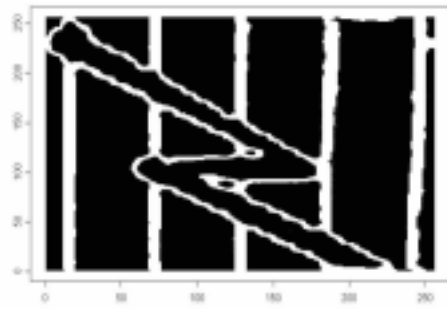
(c)
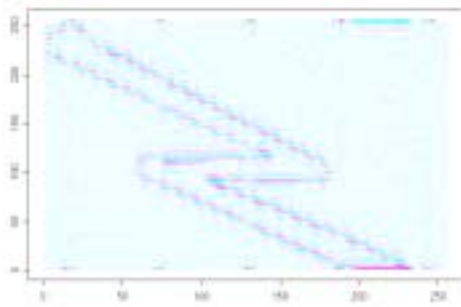
(d)
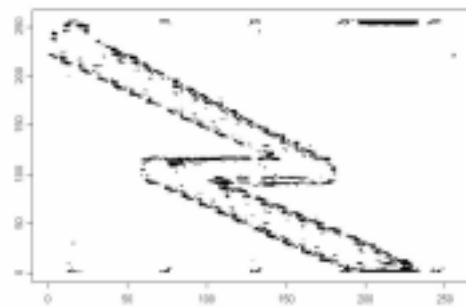
(e)

Figure 14. The effect of selective subimages on image reconstruction for the line-structured texture with a line defect : (a) the original image; (b) the restored image from the smooth subimage; (c) the binarized image of (b); (d) the restored image from the horizontal and diagonal detail subimages; (e) the binarized image of (d).
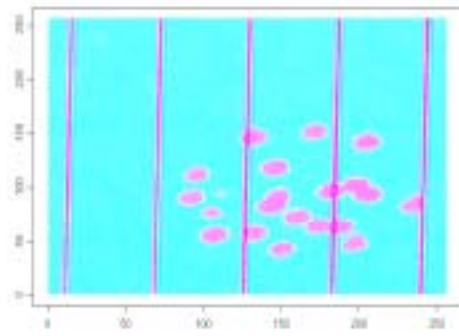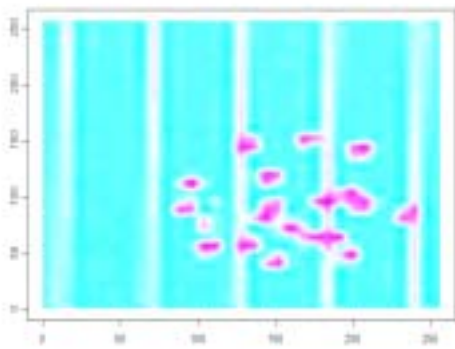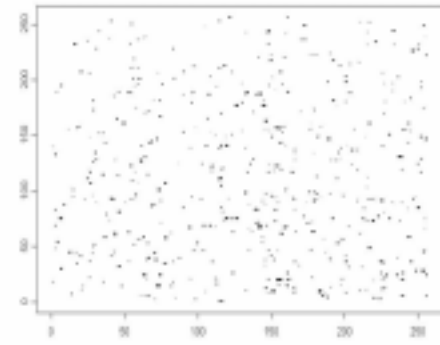
(a) Original image

(b)
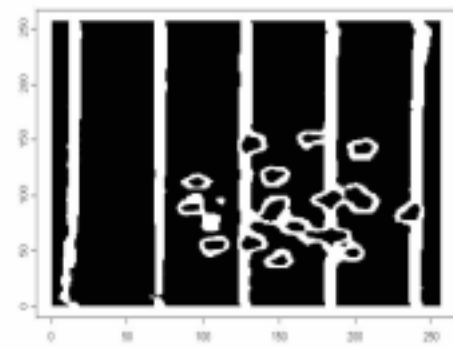
(c)
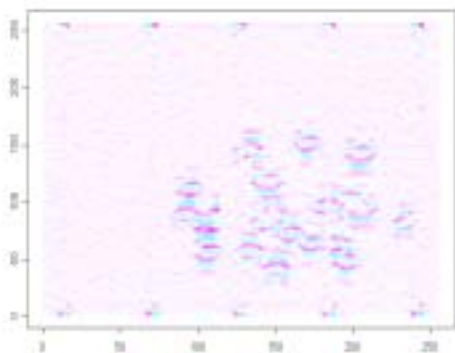
(d)
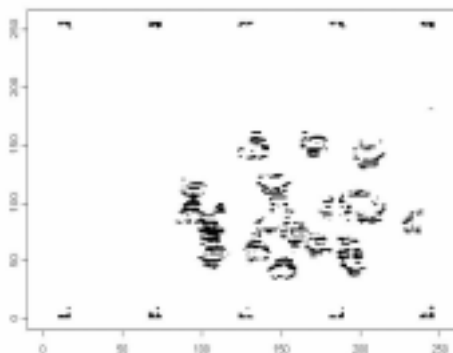
(e)

Figure 15. The effect of selective subimages on image reconstruction for the line-structured texture with blob defects : (a) the original image; (b) the restored image from the smooth subimage; (c) the binarized image of (b); (d) the restored image from the horizontal and diagonal detail subimages; (e) the binarized image of (d).
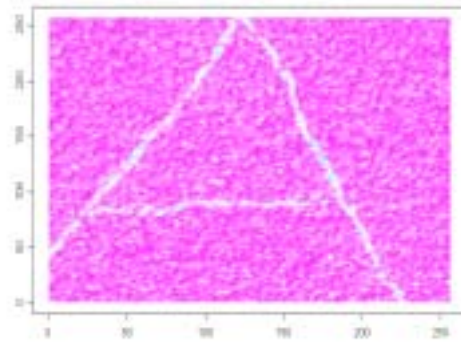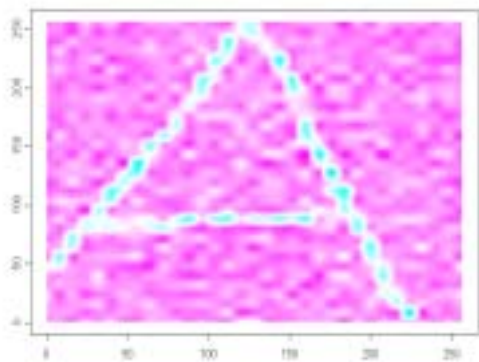
(a) Original image

(b)
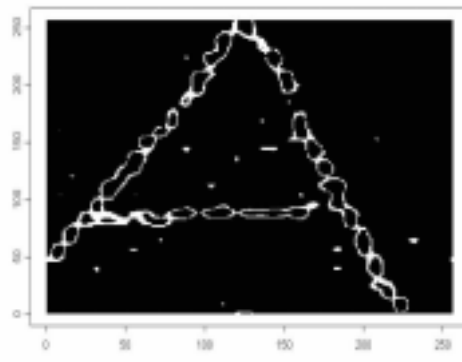
(c)
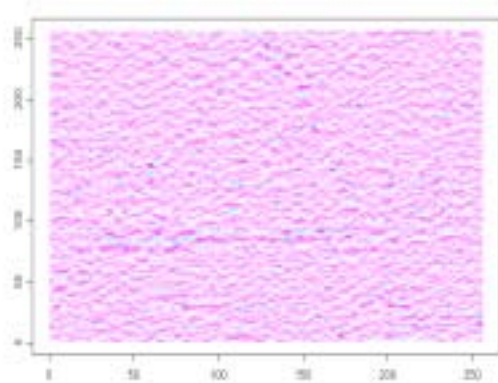
(d)
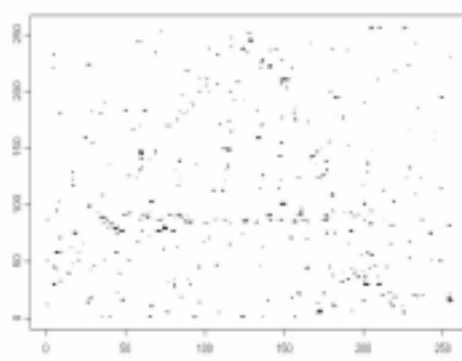
(e)

Figure 16. The effect of selective subimages on image reconstruction for the sandpaper with scratch defects : (a) the original image; (b) the restored image from the smooth subimage; (c) the binarized image of (b); (d) the restored image from the horizontal and diagonal detail subimages; (e) the binarized image of (d).

48
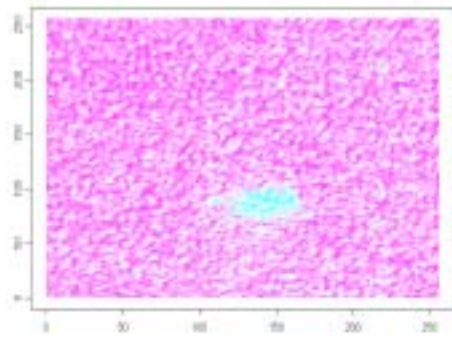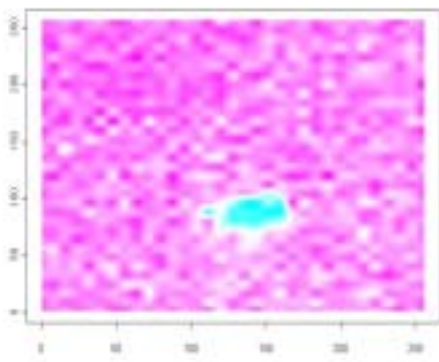
(a) Original image

(b)

(c)

(d)

(e)

Figure 17. The effect of selective subimages on image reconstruction for the sandpaper with a wear defect : (a) the original image; (b) the restored image from the smooth subimage; (c) the binarized image of (b); (d) the restored image from the horizontal and diagonal detail subimages; (e) the binarized image of (d).
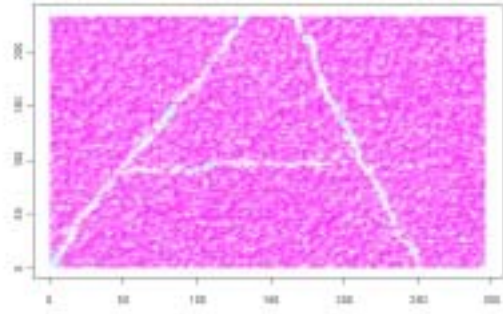
(a)
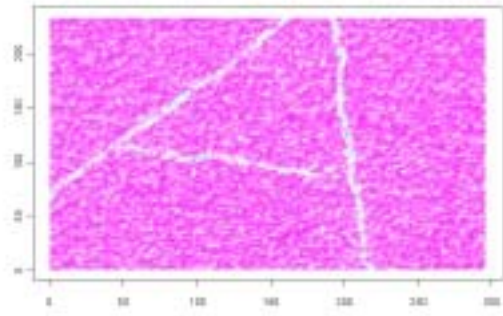
(b)
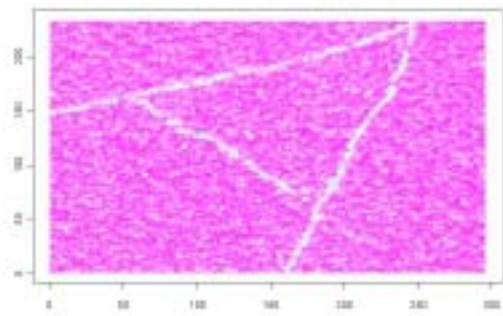
(c)

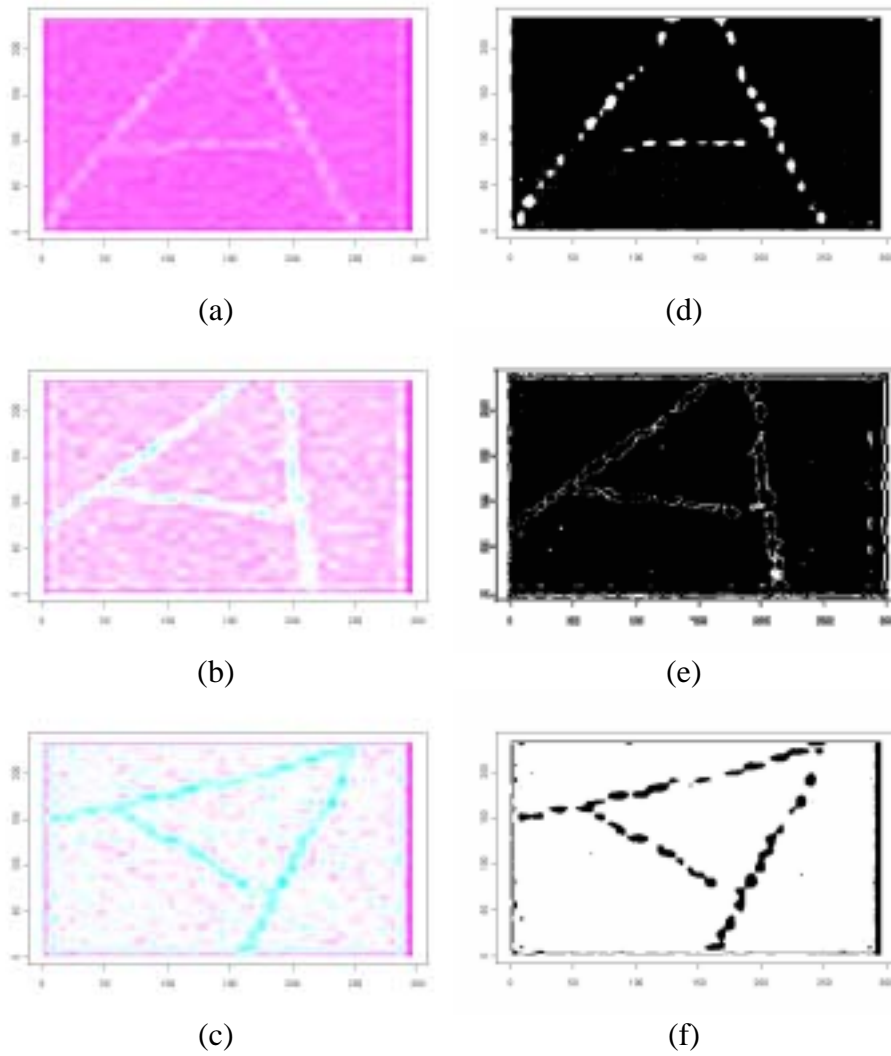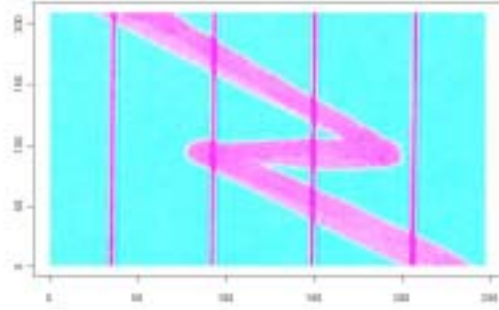Figure 18. A statistical texture of sandpaper in three different orientations.
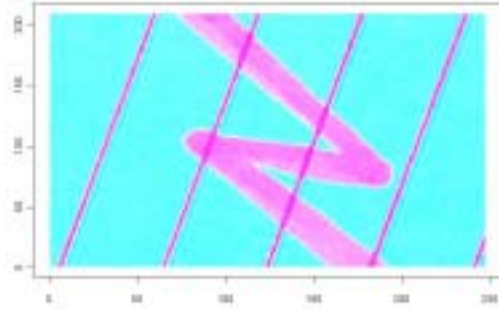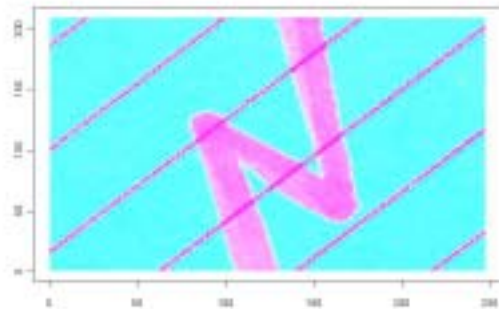
(a)

(d)

(b)

(e)

(c)

(f)

Figure 19. The effect of changes in image rotation for the statistical textures shown in Figure 18: (a), (b), (c) the reconstruction results from the smooth subimages for the sandpaper in three rotations; (d), (e), (f) the corresponding binary images of (a), (b) and (c), respectively.

(a)

(b)

(c)

Figure 20.   A line-structured texture in three different orientations.

(a)   (d)

(b)   (e)

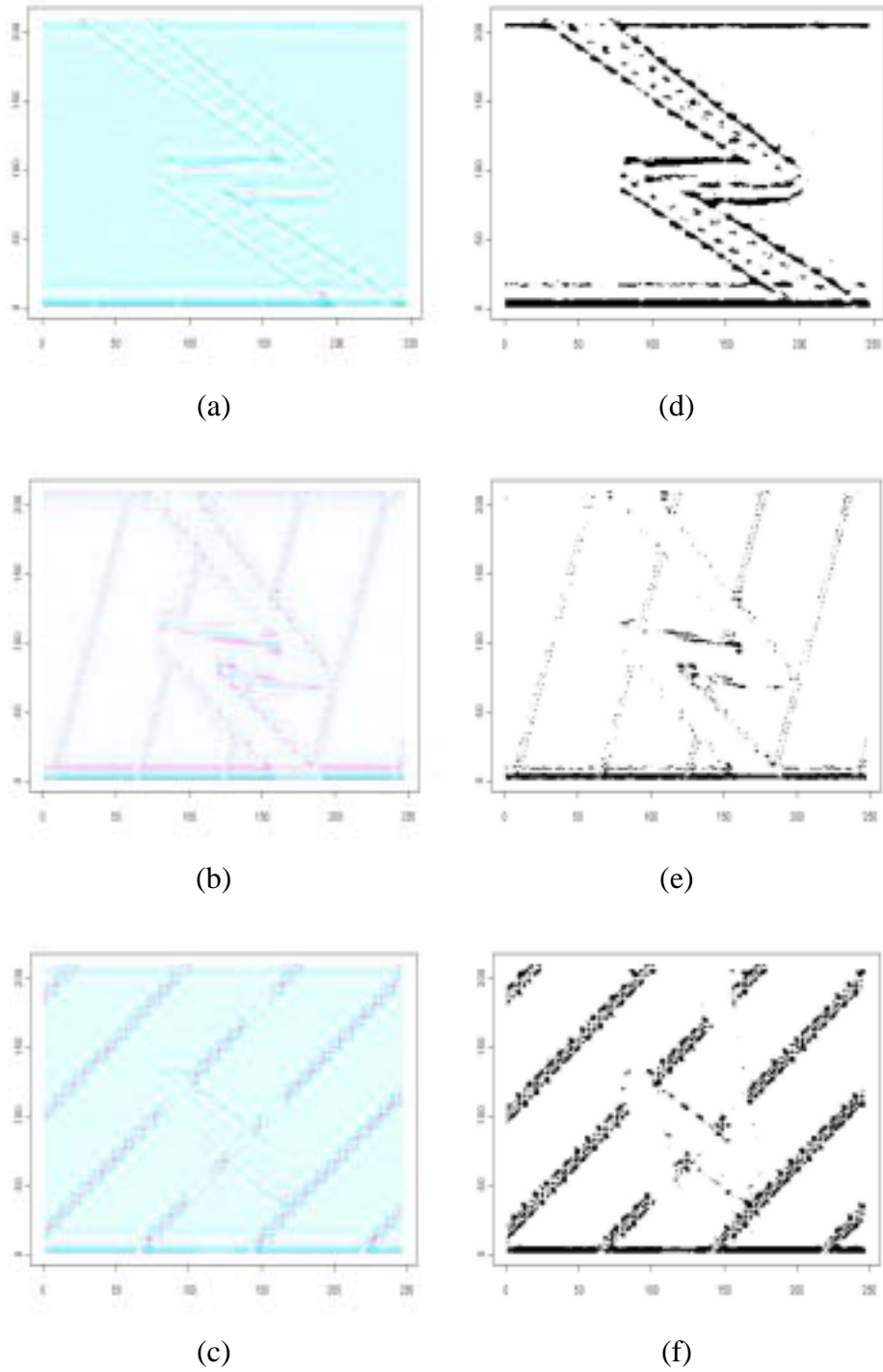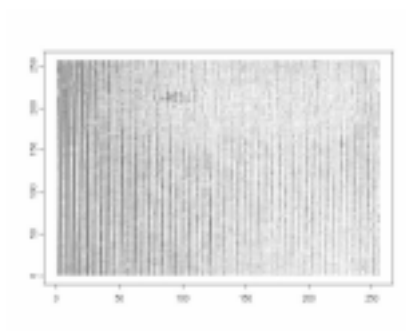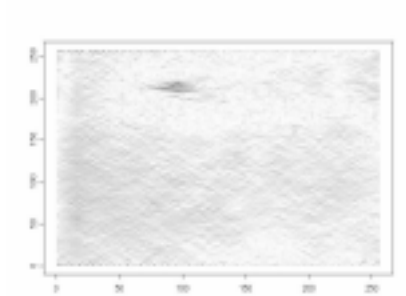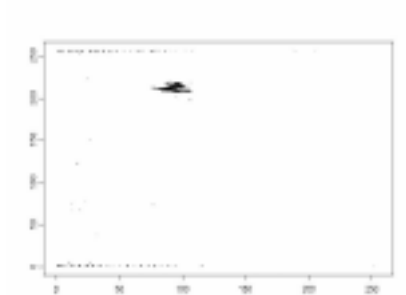(c)   (f)

Figure 21. The effect of changes in image rotation for the structural textures shown in Figure 20: (a), (b), (c) the reconstruction results from the horizontal and diagonal detail subimages for the line-structured texture in three rotations; (d), (e), (f) the corresponding binary images of (a), (b) and (c), respectively.
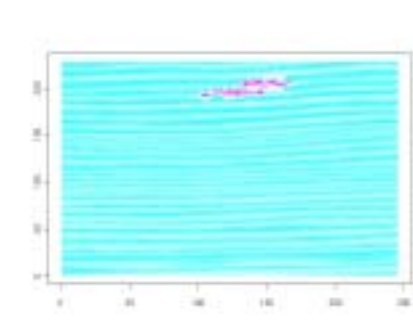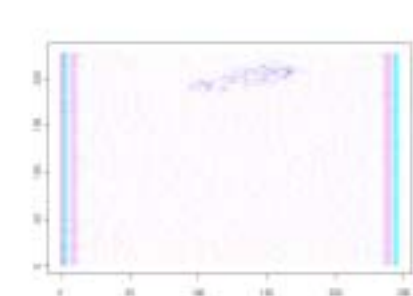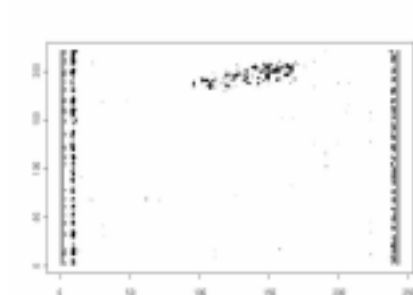
(a)

(a)

(b)

(b)

(c)

(c)

Figure 22. Detecting defects in a milled surface:(a) the original image;(b) the reconstruction result from the horizontal and diagonal detail subimages; (c) the binarized result of (b).

Figure 23. Detecting defects in wood: (a) the original image; (b) the reconstruction result from the vertical and diagonal detail subimages; (c) the binarized result of (b).

(a)   (b)

(c)   (d)

(e)   (f)
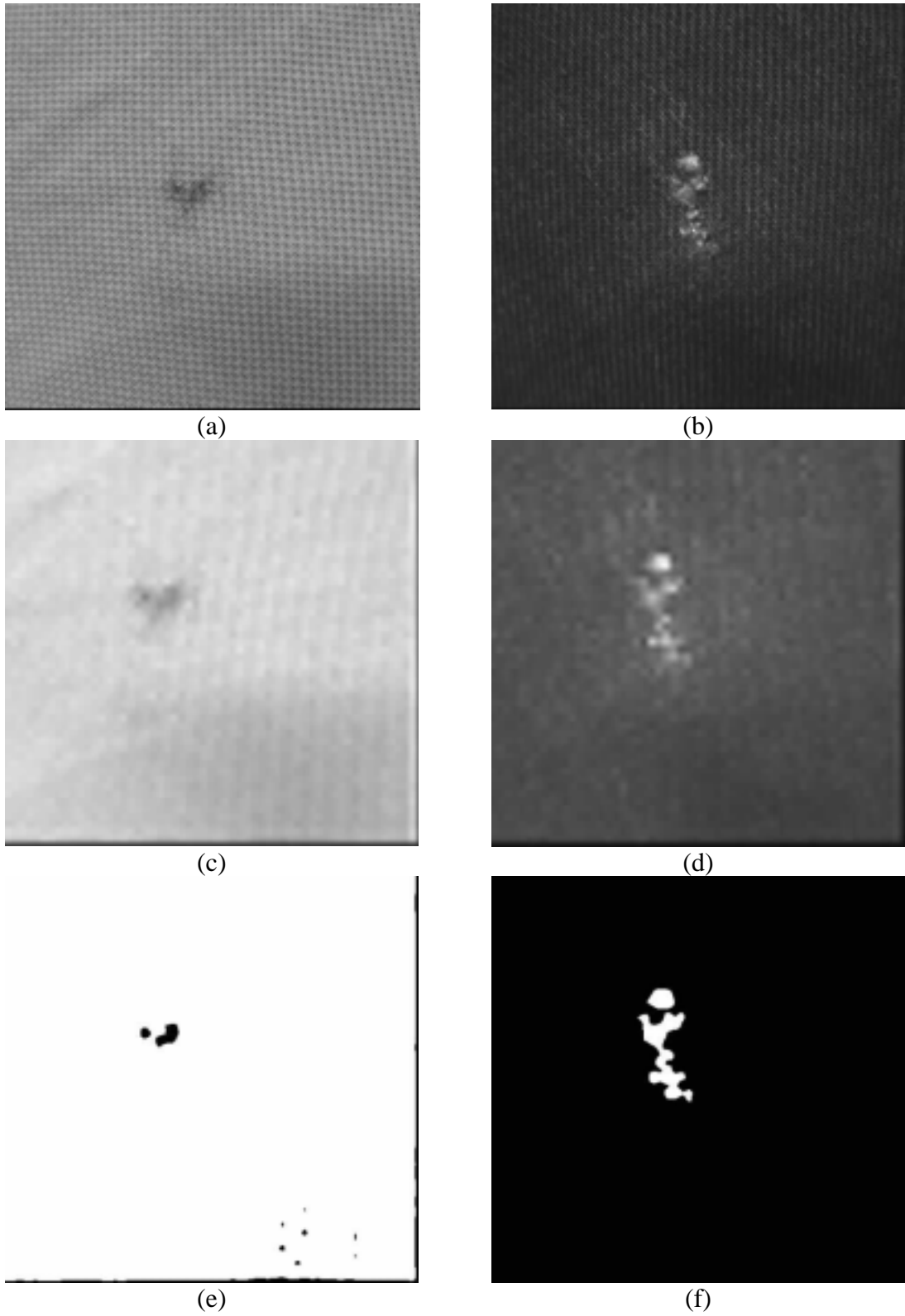
Figure 24. Detecting defects in texture fabrics : (a), (b) two original fabric images; (c), (d) the reconstruction results from the smooth subimages for (a) and (b), respectively; (e), (f) the corresponding binary thresholding results of (c) and (d).

(a)

(b)

(c)

Figure 25. Detecting defects in leather : (a) the original leather image; (b) the reconstruction result from the smooth subimage; (c) the binarized result of (b).

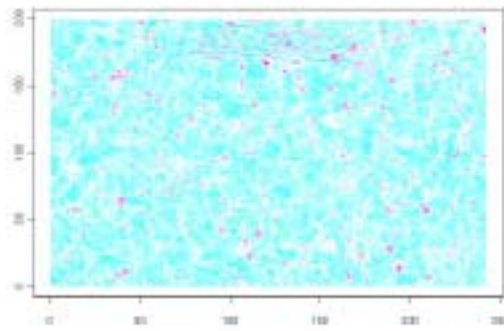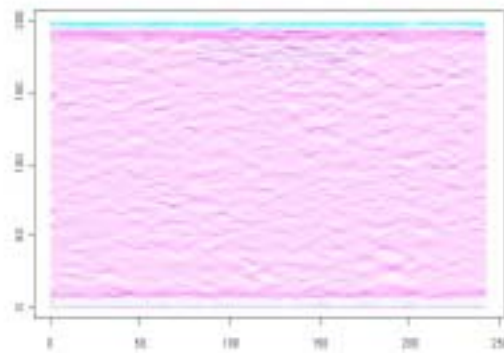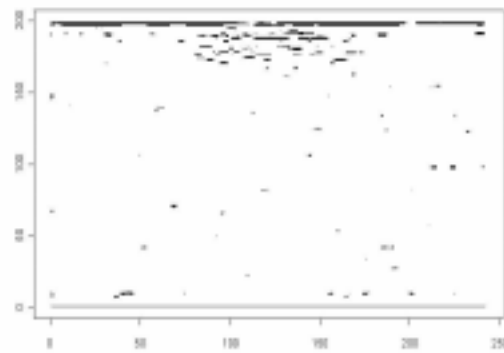(A) Orthogonal wavelet bases

Wavelet basis	Highpass filters $H \quad \tilde{H}$	Lowpass filters $L \quad \tilde{L}$
aar	[00]0.707106781 [01]-0.707106781	[00]0.707106781 [01]0.707106781
D4	[00] 1.2940952255126037 e-01 [01]2.24143868042013390 e-01 [02]- 8.36516303737807940 e-01 [03]4.82962913144534160 e-01	[00].4.82962913144534160 e-01 [01].8.36516303737807940 e-01 [02].2.24143868042013390 e-01 [03].-1.29409522551260370 e-01
D12	[00]-1.077301085000 e-03 [01]-4.777257511000 e-03 [02]5.538422010000 e-02 [03]3.158203931800 e-02 [04]2.752286553000 e-02 [05]-9.750160558700 e-02 [06]-1.297668675670 e-01 [07]2.262646939650 e-01 [08]3.152503517090 e-01 [09]-7.511339080210 e-01 [10]4.946238903980 e-01 [11]1.115407433500 e-01	[00]1.115407433500 e-01 [01]4.946238903980 e-01 [02]7.511339080210 e-01 [03]3.152503517090 e-01 [04]-2.262646939650 e-01 [05]-1.297668675670 e-01 [06]9.750160558700 e-02 [07]2.752286553000 e-02 [08]-3.158203931800 e-02 [09]5.538422010000 e-02 [10]4.777257511000 e-03 [11]-1.077301085000 e-03
S8	[00]0.07576571 [01]-0.02963553 [02]-0.4976187 [03]0.8037388 [04]-0.2978578 [05]-0.09921954 [06]0.0126039 [07]0.0322231	[00]0.0322231 [01]-0.01260397 [02]-0.09921954 [03]0.2978578 [04]0.8037388 [05]0.4976187 [06]-0.02963553 [07]-0.07576571
S20	[00]-0.0004593294 [01]-0.00005703608 [02]0.004593174 [03]0.0008043589 [04]-0.02035494 [05]-0.005764912 [06]0.04999497 [07]0.03199006 [08]-0.03553674 [09]-0.3838268 [10]0.76951 [11]-0.4716907 [12]-0.07088054 [13]0.1594943 [14]0.01160989 [15]-0.04592724 [16]-0.01465383 [17]0.008641299 [18]0.00009563267 [19]-0.0007701598	[00]-0.07088054 [01]0.4716907 [02]0.76951 [03]0.3838268 [04]-0.03553674 [05]-0.03199006 [06]0.04999497 [07]0.005764912 [08]-0.02035494 [09]-0.0008043589 [10]0.004593174 [11]0.00005703608 [12]-0.000459329

(B) Biorthogonal wavelet bases

Wavelet basis	Analysis filters		Synthesis filters	
	Highpass H	Lowpass L	Highpass $\tilde{H}$	Lowpass $\tilde{L}$
Bs1.1	[00]0.7071068 [01]-0.7071068	[00]0.7071068 [01]0.7071068	[00]0.7071068 [01]-0.7071068	[00]0.7071068 [01] 0.7071068
Bs2.2	[00]-0.1767767 [01]-0.3535534 [02]1.06066 [03]-0.3535534 [04]-0.1767767	[00]0.3535534 [01]0.7071068 [02]0.3535534	[00]-0.3535534 [01]0.7071068 [02]-0.3535534	[00]-0.1767767 [01]0.3535534 [02]1.06066 [03]0.3535534 [04]-0.1767767
Bs3.9	[00]0.0006797444 [01]0.002039233 [02]-0.005060319 [03]-0.02061891 [04]0.01411279 [05]0.09913478 [06]-0.01230014 [07]-0.320192 [08]-0.002050023 [09]0.9421257 [10]-0.941257 [11]0.002050023 [12]0.320192 [13]0.0123014 [14]-0.09913478 [15]-0.01411279 [16]0.02061891 [17]0.005060319 [18]-0.002039233 [19]-0.0006797444	[00]0.1767767 [01]0.5303301 [02]0.5303301 [03]0.1767767	[00]-0.1767767 [01]0.5303301 [02]-0.5303301 [03]0.1767767	[00]-0.0006797444 [01]0.002039233 [02]0.005060319 [03]-0.02061891 [04]-0.01411279 [05]0.09913478 [06]0.01230014 [07]-0.320192 [08]0.002050023 [09]0.9421257 [10]0.941257 [11]0.002050023 [12]-0.320192 [13]0.0123014 [14]0.09913478 [15]-0.01411279 [16]-0.02061891 [17]0.005060319 [18]0.002039233 [19]-0.0006797444